Aalto-yliopisto
Sähkötekniikan
korkeakoulu

Tommi Jokela

Hardware-In-the-Loop simulation of an electric vehicle using Energetic Macroscopic Representation

Master's Thesis
Espoo, April 11, 2015

Supervisors: Prof. Anouar Belahcen, Prof. Alain Bouscayrol
Instructor: PhD Walter Lhomme

AALTO UNIVERSITY

SCHOOL OF ELECTRICAL ENGINEERING

MASTER'S THESIS

ABSTRACT

Author:	Tommi Jokela
Title:	Hardware-In-the-Loop simulation of an electric vehicle using Energetic Macroscopic Representation
University:	Aalto University School of Electrical Engineering
Degree Programme:	Electronics and Electrical Engineering
Major:	Electrical drives
Major code:	S3016
Supervisors:	Prof. Anouar Belahcen, Prof. Alain Bouscayrol
Instructor:	PhD Walter Lhomme

Electric vehicles are one of the most promising alternative vehicle propulsion technologies due to their lack of local greenhouse gas emissions and oil dependency. A research project has been put into place to investigate how a commercially existing electric vehicle - the Tazzari Zero - could be modified in order to improve its energetic performance. However, examining different modification possibilities in computer simulation requires a model for the drivetrain of the vehicle. For the goal of describing the energetic performance of the vehicle drivetrain, a static efficiency map model is deemed adequate. An experimental procedure called the on-road efficiency map method has been proposed in order to obtain an efficiency map model for an existing electric vehicle. This is based on instrumenting the vehicle and completing a drive cycle with it. The experimental validation of the on-road efficiency map method is the goal of this Master's Thesis.

The validation of the on-road efficiency map method is performed on a versatile experimental platform that is capable of emulating an electric vehicle following a drive cycle. Hardware-In-the-Loop simulation is used in the implementation of the platform to obtain a good correspondence between the platform and a fully physical electric vehicle. In order to organize the complexity of the platform's design task and to provide a systematic procedure for control design, Energetic Macroscopic Representation is utilized. The validation results show that there is mostly only a minor error of less than 8% in the efficiency map obtained with the on-road method with respect to the efficiency map obtained by the classic protocol.

Date:	April 11, 2015	**Number of pages:** 9 + 74
Language:	English	
Keywords:	Hardware-In-the-Loop simulation, Energetic Macroscopic Representation, electric vehicle, field oriented control	

Tekijä:	Tommi Jokela
Työn nimi:	Sähköauton Hardware-In-the-Loop -simulaatio käyttäen Energetic Macroscopic Representation -metodologiaa
Korkeakoulu:	Aalto-yliopisto Sähkötekniikan korkeakoulu
Tutkinto-ohjelma:	Elektroniikka ja sähkötekniikka
Pääaine:	Sähkökäytöt
Koodi:	S3016
Valvojat:	Prof. Anouar Belahcen, Prof. Alain Bouscayrol
Ohjaaja:	PhD Walter Lhomme

Sähköautoja pidetään yhtenä lupaavimmista vaihtoehdoista tulevaisuuden autojen voimansiirtojärjestelmiksi, koska nämä eivät tuota paikallisesti kasvihuonekaasupäästöjä eivätkä ole suoraan riippuvaisia fossiilisista polttoaineista. Diplomityöhön liittyvä tutkimusprojekti tutkii miten kaupallisesti saatavilla olevan sähköauton - Tazzari Zeron - energiankulutusta voitaisiin parantaa. Eri kehitysvaihtoehtojen tutkimiseksi tietokonesimulaatioiden avulla tarvitaan kuitenkin malli sähköauton voimansiirtojärjestelmälle. Staattinen tehokkuuskartta tarjoaa riittävän tarkan mallin ajoneuvon energiankulutuksen kannalta. Eräs esitetty kokeellinen menetelmä kykenee tuottamaan tällaisen tehokkuuskartan olemassa olevalle sähköautolle. Menetelmä perustuu mittausantureiden asentamiseen ajoneuvoon ja täten tarvittavan datan keräämiseen testiajosta. Käsillä olevan diplomityön tavoite on tämän menetelmän kokeellinen validointi.

Validointi tehdään toteutettavan koejärjestelmän avulla, joka jäljittelee todellisen sähköauton ajonaikaista toimintaa. Jotta tämä koejärjestelmä vastaisi hyvin todellisen sähköauton toimintaa, se toteutetaan Hardware-In-the-Loop -simulaatiota hyväksi käyttäen. Koejärjestelmän laajuudesta ja haastavuudesta johtuen teoreettisena apuvälineenä käytetään Energetic Macroscopic Representation -metodologiaa. Tämä helpottaa järjestelmän matemaattisen mallin jäsentämistä ja tarjoaa systemaattisen proseduurin säätösuunnitteluun. Validointitulokset osoittavat, että validoitavan menetelmän ja vastaavan perinteisen metodin tuottamien tehokkuuskarttojen välinen ero on pieni, enimmäkseen alle 8%.

Päivämäärä:	11. huhtikuuta, 2015 **Sivumäärä:**		9 + 74
Kieli:	Englanti		
Avainsanat:	Hardware-In-the-Loop -simulaatio, Energetic Macroscopic Representation, sähköauto, vektorisäätö		

Foreword

First and foremost, I would like to thank my supervising professors Anouar Belahcen of Aalto University and Alain Bouscayrol of Université Lille 1 who gave me the opportunity to write my Master's Thesis at Laboratoire d'électrotechnique et d'électronique de puissance (L2EP) in Lille, France. I am grateful to professor Bouscayrol for assigning me such a challenging and intriguing research subject. I have had an excellent environment to perform research and to deepen my knowledge on many aspects of electrical drives, vehicular technology, real-time simulation and control systems as well as developing a systems level view of things. I would also like to thank my Master's Thesis instructor at L2EP, associate professor Walter Lhomme for providing a very friendly working environment and valuable practical advice and ideas related to the work. In general, I wish to express my thanks to all the staff of L2EP for having made me feel welcome in the team in Lille right from the beginning.

All of the experimental results of this work were obtained in close collaboration with doctoral candidate Clément Dépature of L2EP. In particular, Clément has provided the original efficiency maps of this work based on our experimental results. My sincere thanks go to Clément for giving me excellent guidance to the practical aspects of working in the L2EP laboratory, as well as always being open to discussion and ideas while working on the implementation of the emulation platform.

Finally, I wish to express my profound appreciation and gratitude for the tireless and selfless support of my family and Mathilde during the past years. It continues to mean a lot to me.

April 2, 2015 in Naantali, Finland

Tommi Jokela

Contents

Symbols and abbreviations

Symbols

A	Vehicle frontal area (m^2)
B_{tot}	Equivalent friction coefficient of shaft (Ns/m)
c_x	Coefficient
$\underline{e}_x$	Back emf in dq coordinates (V)
f	Friction coefficient of shaft (Nms)
F_x	Force (N)
g	Standard gravitational acceleration (m/s^2)
i_x	Current (A)
j	Complex unit
J	Moment of inertia of rotational movement (kgm^2)
k	Power direction indicator
k_x	Reduction ratio
k_d	Braking force distribution parameter
K	Space vector scaling constant
K_x	Transfer function static gain
L_x	Inductance (H)
$\underline{m}$	Modulation function vector controlling VSI switching
m_x	Mass (kg)
M_{sr}	Mutual inductance between stator and rotor of induction machine (H)
M_{tot}	Total equivalent mass of the vehicle including rotational inertia (kg)
p	Pole pair number
P_x	Power (W)
r_{wh}	Wheel radius (m)
R_x	Resistance (Ω)
$\Re\{\cdot\}$	Real part operator
s	Laplace variable
s_x	Switching order of semiconductor switch
t	Time (s)
T_x	Torque (Nm)
$[T_i]$	Operator yielding machine phase currents from inverter line currents
$[T_{ii}]$	Operator yielding inverter line currents from machine phase currents
$[T_{uv}]$	Operator yielding machine phase voltages from inverter line-to-line voltages
$[T_{vu}]$	Operator yielding inverter line-to-line voltages from machine phase voltages
u_x	Voltage of inverter, battery or DC bus (V)

v_x	Voltage of electrical machine (V)
v_{veh}	Vehicle velocity (m/s)
v_{wind}	Wind velocity against vehicle (m/s)
α	Slope angle (deg)
η_x	Efficiency
θ_x	Transformation angle (deg)
ρ	Air density (kg/m^3)
σ	Leakage factor of induction machine
τ_x	Transfer function time constant (s)
$\underline{\Phi}_x$	Flux (Wb)
ω_x	Electrical rotation angular frequency (rad/s)
Ω_{sh}	Mechanical rotation angular frequency of shaft (rad/s)

Subscripts

x_{ave}	Average
x_b	Mechanical brake
x_{bat}	Battery
x_{bus}	DC bus
x_d	d component of variable expressed in the dq coordinate system
x_{diff}	Mechanical differential
x_{dq}	dq coordinate variable
x_{drag}	Drag
x_{drive}	Electrical drive
x_{dt}	Drivetrain
$x_{d/r}$	From rotor coordinates to dq coordinates
$x_{d/s}$	From stator coordinates to dq coordinates
x_{env}	Environment
x_{est}	Estimated quantity
x_{full}	Full power level
x_{gear}	Gear
x_{im}	Induction machine
x_{in}	Input
x_{inv}	Inverter
x_L	Load
x_{meas}	Measured value
x_{nom}	Nominal value

x_{out}	Output
x_{pm}	Permanent magnet
x_q	q component of variable expressed in the dq coordinate system
x_r	Rotor
x_{ref}	Reference value
x_{res}	Resistive
x_{roll}	Rolling
x_s	Stator
x_{sm}	Synchronous machine
x_{tract}	Traction
x_T	System under test
$x_{\alpha_r \beta_r}$	Rotor coordinate variable
$x_{\alpha_s \beta_s}$	Stator coordinate variable

Abbreviations

COG	Causal Ordering Graph
EIS	Emulation Interface System
EM	Electrical Machine
EMR	Energetic Macroscopic Representation
EV	Electric Vehicle
HIL	Hardware-In-the-Loop
IBC	Inversion-Based Control
IM	Induction Machine
MCS	Maximum Control Structure
PMSM	Permanent Magnet Synchronous Machine
PWM	Pulse Width Modulation
SM	Synchronous Machine
SUT	Subsystem Under Test
VSI	Voltage-Source-Inverter

1 Introduction

Electric vehicles (EV's) are currently undergoing major development as the emissions and oil dependency issues of combustion engine vehicles increase in significance [1, 2]. Indeed, EV's have the potential to significantly reduce or to completely eliminate these problems. In order to advance the development of EV's, a research project has been put into place that aims to find improvements to a commercially existing electric vehicle - the Tazzari Zero. Computer simulations are an important initial phase in investigating the different possibilities of improving the vehicle. However, this requires a model that describes the behaviour of the vehicle in simulation. Given that the research project aims at improved energy economy of the vehicle, a static efficiency map model has been deemed sufficient.

Unfortunately, conventional methods cannot be used on the Tazzari Zero to obtain an efficiency map for the drivetrain. This is because the electric traction drive's operating point cannot be controlled accurately while driving the vehicle. To overcome this problem, an experimental method of obtaining the efficiency map of an existing electric vehicle has been proposed [3]. This is done based on measurements performed on the vehicle during a drive cycle. However, this method has not been validated experimentally. This validation is defined as the goal of this Master's Thesis.

The Master's Thesis is organized as follows. Chapter 2 gives the context of the work and defines the approach towards achieving this goal. The validation is done by forming an experimental platform that is capable of emulating an EV following a drive cycle. In this way, the experimental efficiency map method can be used on the platform just as on a real vehicle. In addition - and in contrast to a real vehicle - the platform also enables using the classic protocol of measuring an efficiency map for an electrical drive. Consequently, the validation can be done by comparing the efficiency map from the experimental method to the efficiency map obtained from the classic protocol. Chapter 3 describes the implementation of the emulation platform. A Hardware-In-the-Loop (HIL) simulation [4, 5] implementation is chosen because it enables the platform to have a high correspondance to a real vehicle while still retaining the required flexibility. Consequently, implementing the emulation platform requires not only modeling and control of the drivetrain but also taking into account how the HIL implementation's physical and real-time simulated parts interact. To organize the complex mathematical model of the platform and to design its control, Energetic Macroscopic Representation [6] is chosen as a well-adapted tool. Chapter 4 presents the experimental results of the validation, i.e. the two efficiency maps and their comparison. Chapter 5 concludes the work and offers perspectives.

2 Research project and approach taken

The automotive industry is currently undergoing major change due to the problems related to conventional thermal vehicles. The main issues of these vehicles are greenhouse gas emissions and dependency on increasingly limited oil resources [7, 8]. Alternative technologies such as electric, hybrid and fuel cell vehicles have been proposed and are being widely developed at the moment [1]. Out of these alternatives, electric vehicles have several key advantages. They completely eliminate local greenhouse and other noxious gas emissions as well as the fossil fuel dependency[1]. Furthermore, the peak and overall energy efficiencies are superior to alternatives and the EV drivetrain has need for fewer mechanical parts than thermal vehicles. However, although the EV market has witnessed a dramatic increase in the availability of mass production models [13], the widespread consumer adoption of EV's has been slow. This is due to battery-related issues such as vehicle autonomy, charging issues, battery lifetime and initial cost [14]. Consequently, considerable research has been devoted recently to these issues [15, 16, 17, 18] and the industry has been actively promoting alternative selling policies to offset high initial prices.

This work is part of a research project that aims to contribute to the field. The energetic performance of electric and hybrid electric vehicles is investigated to find improvements to these technologies. In this type of studies, computer simulation is an important tool to conveniently and safely examining the performance of different configurations of the vehicle [2, 19]. However, this requires a model that adequately describes the behaviour of the vehicle. The used model type and accuracy should be chosen in view of the goal and constraints of the work. Here, for the goal of investigating energetic performance of the vehicle, a static model is chosen as sufficient. In the research project related to this work, one of the key ideas is to investigate a specific, existing electric vehicle. This is a commercially available electric vehicle - the Tazzari Zero, shown below in figure 2.1. In this way, the research efforts gain a higher level of interest since there is a direct reference point in a commercial application. Due to the somewhat unusual requirement of modeling an already existing EV, some kind of a test procedure is needed to obtain the required static model. An experimental method for accomplishing this has been proposed in [3] but the method has not been experimentally validated. Thus, the validation of this method is defined

---

[1]Extensive life cycle assessment studies have recently been made to compare the greenhouse gas emissions of electric vehicles to those of conventional vehicles. In addition to actual vehicle usage, they take into account factors such as electricity production, vehicle manufacturing and end-of-life issues. Typically it is found that unless electricity production is heavily dominated by fossil fuels, EV's result in significantly lower levels of greenhouse gases during their lifetime than conventional vehicles [9, 10, 11, 12].

Figure 2.1: Tazzari Zero.

as the goal of this Master's Thesis. Should the method be validated, the Tazzari Zero static model would become available for use in further studies. For example, structural modifications such as adding supercapacitors [20] or fuel cells [21] to obtain a hybrid energy storage system [22] could be investigated. The goal of this chapter is to give the context of the research project, define more precisely the goal of the Master's Thesis and to give an outline of how this goal will be reached.

2.1 Vehicle of interest: Tazzari Zero

To ensure industrial applicability of the research efforts, this project focuses on the study of a commercial four-wheeler EV - the Tazzari Zero [23] whose drivetrain is illustrated below in figure 2.2. The vehicle's 15kW induction machine (IM) is supplied by a Lithium Iron Phosphate (LiFePO4) battery pack with 160Ah storage capacity at a voltage level of 80V through a three-phase inverter. The machine shaft speed is reduced by a single fixed ratio gearbox and the rotational torque is distributed to the two driven wheels by the mechanical differential. The wheels are equipped with mechanical brakes due to the limited regenerative braking capacity possible with the
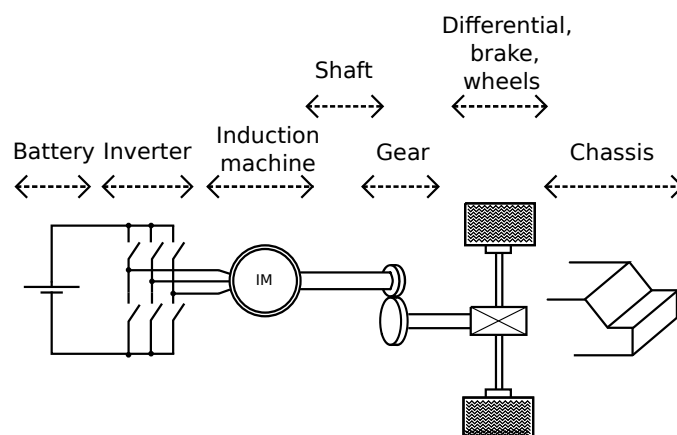

Figure 2.2: Tazzari Zero drivetrain.

electrical machine (EM) and for safety. Finally, the mass of the vehicle represented by the chassis, stores kinetic energy of the vehicle and it is thus considered to be a part of the drivetrain. The vehicle has been instrumented to provide measurements of the battery voltage and current as well as GPS data from which the velocity and altitude of the vehicle can be deduced. The empty mass of the vehicle including the instrumentation system is 562kg. Further details about the Tazzari Zero and its instrumentation are given in appendix A.

As explained, to be able to investigate improvement possibilities to the vehicle through computer simulations, a model for it is required. One possibility and the one employed in this project is the use of *efficiency maps* that are often used to characterise variable-speed electrical drives [24, 25]. Variable-speed applications such as electrical traction need to operate efficiently at a range of different operating points as opposed to typical industrial applications operated with nominal voltage supply. The efficiency of variable-speed drives can be conveniently presented in the form of an efficiency map that is simply the collection of steady state operating efficiencies plotted in the torque-speed plane.

The current IEEE standard [26] does not specify a measurement protocol for the efficiency of variable-speed IM drives. Rather, an efficiency measurement protocol is given only for the electrical machine supplied at the rated voltage and frequency at varying loads. A logical extension to variable-speed drives, as proposed in [25], would be the use of an efficiency map constructed by measuring efficiencies at different torque-speed combinations. The test setup to accomplish this is shown in figure 2.3. In this work it is referred to as the *classic efficiency map protocol*. Two electrical machines are connected to the same shaft. Each has dedicated power electronic converters and control algorithms. The actual test drive is controlled for torque T_T while the load drive is controlled for shaft rotation speed Ω_{sh}. Consequently, all operating
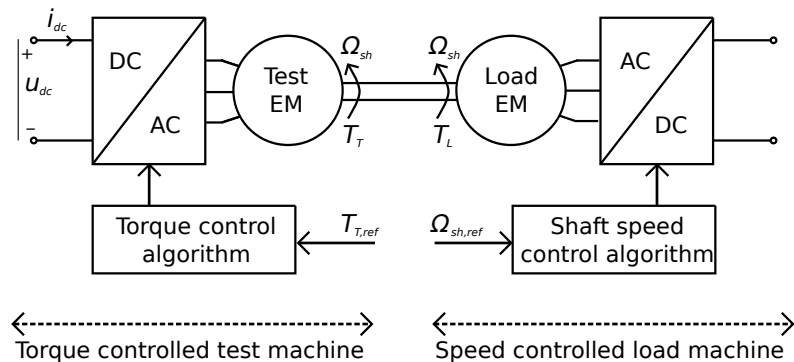

Figure 2.3: Efficiency map classic protocol measurement setup.

points can be covered by systematically changing the reference values $\{T_{T,ref}, \Omega_{sh,ref}\}$. For each of these operating points an efficiency is computed according to

$$\eta_{drive} = \frac{P_{out}}{P_{in}} = \frac{T_T \Omega_{sh}}{u_{dc} i_{dc}} \qquad \text{[(2)-1]}$$

Thus, measurements of the test drive's DC bus current and voltage as well as the machine torque and shaft rotation speed are needed. The finite number of operating points recorded can then be extended to a continuous efficiency map by means of interpolation and extrapolation [27].

It should be stressed that an efficiency map constructed as above is a model not only for the test machine but that it includes also the efficiency of the power electronic converter and the effect of the torque control algorithm[2]. Moreover, it is a static model that describes only steady state operation, thus neglecting transient states. Despite this limitation, it is quite sufficient for energetic studies of drive systems also in applications such as traction where operation is in transient states a major part of the time.

Unfortunately, this protocol cannot be utilized to obtain an efficiency map for the Tazzari Zero. This would require removing the electrical drive from the vehicle and installing it in a test bench of the type described in figure 2.3. Such a procedure would make the vehicle illegal to drive afterwards in France, not to mention the impracticality of the procedure. Therefore, a less radical method of determining the Tazzari Zero efficiency map is desired. This is the subject of the following subsection.

2.2   On-road efficiency map method

A non-invasive method has been proposed in [3] in order to obtain the efficiency map for an existing EV without invasive and impractical operations. This *on-road efficiency map method* uses measurement data recorded from completing a drive cycle with the vehicle. This data is then used to deduce an efficiency map. It does not require modifications to the vehicle other than instrumenting it with battery voltage and current sensors as well as a GPS antenna that can provide velocity and altitude data of the vehicle. Assuming that the driving cycle is varied enough, a sufficient number of different operating points is recorded to construct an efficiency map. The efficiencies for each of the recorded operating points can be calculated with a modified version of [(2)-1]. Here, the output mechanical power is written as the linear movement power of the vehicle instead of the rotational movement of the shaft. The

---

[2]This is why the term *electrical drive* is preferable to only discussing the electrical machine.

efficiency for a given operating point can thus be written as

$$\eta_{dt} = \frac{P_{out}}{P_{in}} = \frac{F_{tract}v_{veh}}{u_{bat}i_{inv}}$$ [(2)-2]

with F_{tract} the traction force generated by the drivetrain, v_{veh} the vehicle speed, u_{bat} the battery voltage and i_{inv} the inverter DC side current. In contrast to the efficiency described by equation [(2)-1], this includes the efficiency of not only the electrical drive and its control but also the fixed ratio gearbox, the differential and the wheels. Because the instrumentation system does not include a dynamometer, the traction force F_{tract} is not directly measured but estimated. This is accomplished with Newton's second law

$$M_{tot}\frac{d}{dt}v_{veh} = F_{tract} - F_{env}$$ [(2)-3]

where F_{env} is the resistive force of the environment and M_{tot} the total equivalent mass of the vehicle[3]. Here, the resistive force is estimated to be composed of a rolling resistance, air resistance and a grade force according to

$$F_{env} = c_{roll}M_{tot}g + \frac{1}{2}\rho c_{drag}A(v_{veh} + v_{wind})^2 + M_{tot}g\alpha$$ [(2)-4]

where c_{roll} is the rolling resistance coefficient, g is the standard gravitational acceleration, ρ the air density, c_{drag} the drag coefficient, A the frontal area of the vehicle, v_{wind} the wind velocity against the vehicle and α the slope angle. Thus, the estimated traction force $F_{tract,est}$ can be obtained using [(2)-3] and [(2)-4]. The parameter values used for the Tazzari Zero are presented in appendix A. Combining the estimation $F_{tract,est}$ with measurement data consequently allows using equation [(2)-2] to compute the efficiency for each recorded operating point. Then, interpolation and extrapolation allow obtaining a continuous efficiency map.

However, there are multiple potential sources of error related to the method. First, the operating point measurements are not recorded in steady state operation like in the classic protocol. The vehicle speed and the drivetrain traction force are constantly changing as required by the drive cycle. This dynamic error could potentially have a significant distorting effect on the efficiency map. Second, the traction force estimation requires the knowledge of many environmental and vehicle parameters. Errors in these parameters could also have degrading effects on the resulting efficiency map. The environmental force estimation is also affected by the GPS speed and slope mea-

---

[3]The total equivalent mass includes the actual mass of the vehicle and the equivalent mass of the rotational inertia of the drivetrain.

surement error. Finally, the numeric derivation required in the estimation can also lower the accuracy of the traction force estimate. Due to these potential sources of error, the on-road method should be experimentally validated before using the resulting efficiency map in other research efforts.

An example of an efficiency map deduced for the Tazzari Zero obtained with this method is shown in figure 2.4. The black dots represent measured operating points from the drive cycle while the rest of the values are results of interpolation and extrapolation. The drive cycle that was used to obtain this map was an extra-urban drive cycle and thus operating points have been recorded from most parts of the force-speed plane. Two operating regions can be clearly distinguished from the efficiency map. First, at speeds lower than the base speed, the maximum force (thick black line) remains constant regardless of the speed. Here, the highest traction power is obtained at the maximum speed and force before the force producing capability starts to decrease at approximately $8.1 m/s$ and $1867 N$. Second, at speeds higher than this, the IM enters field weakening operation. Here, the maximum torque capability of the machine decreases as the inverse of the speed increase. Thus, the maximum power is constant in this region. Induction machine drives typically have optimal efficiencies at moderate field weakening speeds with relatively low torques [24, 25]. The discrepancies with the Tazzari Zero efficiency map may be due to the quite different type of induction machine drive in the Tazzari Zero (see appendix A) when comparing to typical industrial drives. Traction drives need to operate efficiently at various torque and speed combinations while an industrial drive is typically run mostly close to the
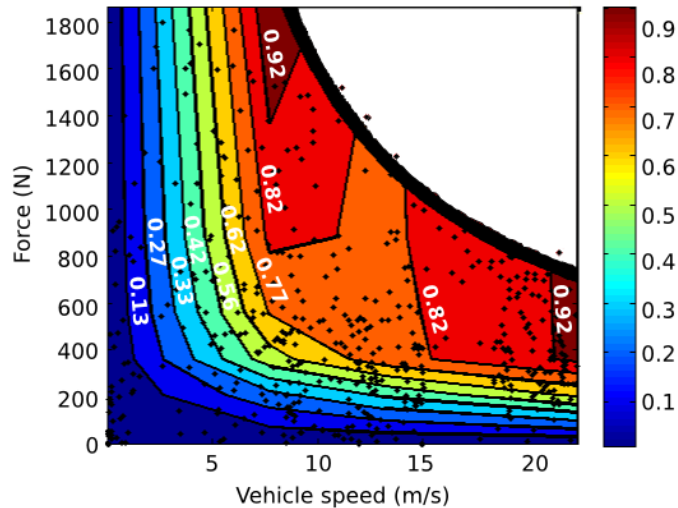

Figure 2.4: Efficiency map of the Tazzari Zero drivetrain obtained by using the on-road efficiency map method.

nominal speed. Thus, it seems very probably that the Tazzari Zero electrical drive has been optimized with this in mind. In addition, the inclusion of the efficiencies of the mechanical parts could also have the effect of changing the efficiency distribution in the efficiency map. Finally, it is noted that the quality of the on-road method's efficiency map depends on the drive cycle. For operating regions where few or no operating points are measured, the method must rely more heavily on interpolation and extrapolation. Since this leads to an increased risk of error, the on-road method should be used on a drive cycle that is highly varied. For the efficiency map of figure 2.4, the low number of operating points recorded at speeds of 12-14 m/s and high torque may explain why the zones of highest efficiencies (efficiency contour of 82%) has been divided in two. Note that the efficiency map includes only positive traction forces. This is because the Tazzari Zero's strategy of partitioning braking force into regenerative braking and into mechanical braking is unknown. Thus, operating points from braking phases ($\frac{dv_{veh}}{dt} < 0$) are not included in the efficiency map.

The on-road efficiency map method would provide a useful tool for future works that require a model for the Tazzari Zero. However, due to the many underlying uncertainties of the method, it needs experimental validation. This is defined as the goal of this Master's Thesis. In this work, focus is given in particular to investigating if the dynamic measurement conditions of the on-road method have a significant distorting effect on the efficiency map. The following approach is taken to accomplish the validation. An experimental platform capable of emulating the behaviour of the Tazzari Zero following a drive cycle is constructed. Consequently, the on-road efficiency map method can be employed on this platform to deduce the efficiency map of the emulated traction drive. However, in addition it will also allow modifications to be conveniently made in order to construct a reference efficiency map. This can be accomplished by using the equivalent of the classic protocol presented in figure 2.3. Thus, the on-road efficiency map method could be validated by a high similarity between these two efficiency maps. It is the subject of the remainder of this chapter to outline how this emulation platform can be formed.

2.3   Validation using Hardware-In-the-Loop simulation

As noted above, the on-road efficiency map method could be validated by using an emulation platform. This platform has two main requirements. First, it must be able to emulate the behaviour of an electric vehicle following a drive cycle. This emulation capability then allows employing the on-road method on the emulation platform. In this way, an efficiency map can be deduced much in the same way as for the real Tazzari Zero. Second, the emulation platform must be easily modifiable so that an

equivalent of the classic protocol can also be accommodated by the platform. In this way, the classic protocol can be used to obtain a reference efficiency map. Should the two efficiency maps be highly similar, the on-road method would be validated.

A well adapted approach to fulfilling these two requirements is *Hardware-In-the-Loop simulation*. This entails using one or several physical devices in conjuction with real-time simulated mathematical models [4, 5]. Thus, it represents an intermediary stage between software simulation (only mathematical models) and a physical system (only physical equipment). It is well suited to the needs of this work for the following reasons. First, it allows employing the on-road method on a real system whose behaviour corresponds well to the actual Tazzari Zero. Second, an HIL simulation implementation provides the required flexibility to also accommodate the classic protocol.

In any HIL simulated system, the most fundamental choice is deciding which system components are implemented by physical equipment and which components by real-time simulated mathematical models. The appropriate choice depends on the goal of the setup. Often, HIL simulation is used in the industry[4] as a tool in the design and testing of a system or product. The physical components of the system are then typically the subsystem under test (SUT) while the simulated parts allow testing of the SUT as a part of the whole system in realistic conditions. By increasing the number of physical components in the system, HIL simulation thus enables the gradual progression from a computer simulation model to a fully physical prototype.

However, the goal of this work is not to design a new system but to validate the on-road efficiency map method. The requirement of high correspondancy of the emulation platform with a physical EV means using a maximum number of physical components in the system. This is because any mathematical model is always an approximation of the system that it describes. Furthermore, the simulation of such models is performed with a finite simulation time step as opposed to the continuous nature of most real processes. Decreasing the simulation step size decreases the resulting error but this can only be done up to the limit set by the available computational capacity. On the other hand, the flexibility of the platform that is needed to accommodate the classic protocol decreases as the number of used physical components increases. Especially the mechanical parts of the drivetrain shown in figure 2.2 are impractical in terms of actual implementation. Therefore, the following choice is taken in dividing the HIL implementation into physical and simulated parts. The

---

[4]Usage has been popular especially in the aerospace [4] and automotive [28] industries where there are extreme constraints related to safety or development time. Indeed, HIL simulation testing allows extensive testing of a system in a wide variety of operating conditions while reducing overall development time and costs.

electrical parts including the induction machine shall be implemented by physical equipment while the remaining mechanical parts are simulated according to mathematical models. This is illustrated below in figure 2.5. Due to the simulation of the mechanical parts, there will be some level of discrepancy between the simulated behaviour and what would be the behaviour of actual physical parts. The magnitude of this error depends on the model chosen to implement these parts.

Due to the different nature of the physical and simulated parts, an emulation interface system (EIS) is required [5]. This interface exchanges power variables with the physical part and signal variables with the simulated part. The physical and simulated parts of the drivetrain are controlled by a real-time controller based on the control reference and measurements from the physical and simulated parts of the drivetrain[5].
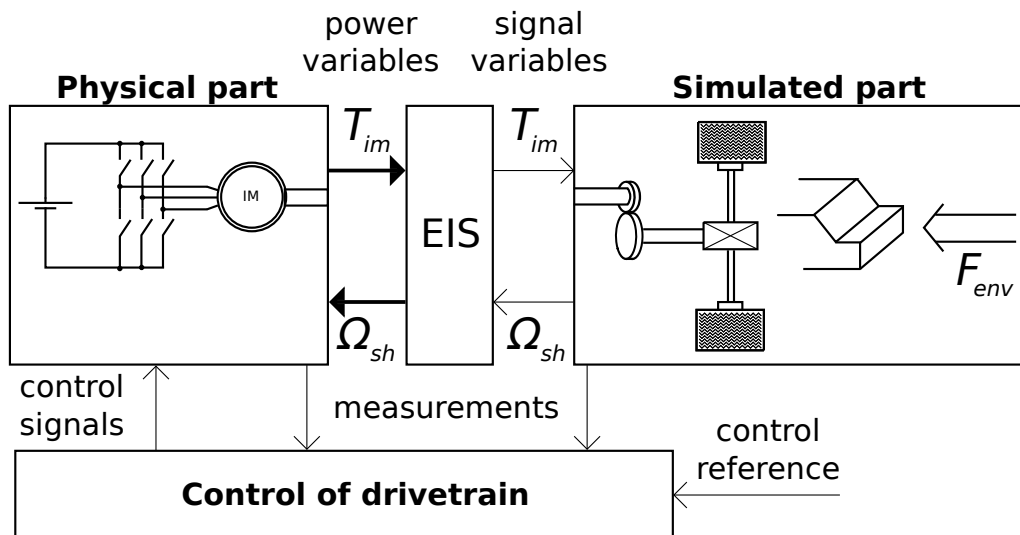

Figure 2.5: Emulation platform implementation by HIL simulation.

The EIS has the important responsibility of acting as the interface between the physical and numeric domains. It has the same variables as its inputs and ouputs but needs to translate the nature of these variables between physical quantities and their corresponding numeric values. First, the physical torque of the induction machine T_{im} needs to be translated to a numeric value. One way to accomplish this is simply to measure the torque with a dynamometer. Second, the EIS is required to accept the numeric shaft rotation speed value Ω_{sh} from the simulated part and actuate it physically onto the induction machine shaft. This shaft speed is the response of the

---

[5]Note that for the control operation it is not relevant which parts are implemented by physical components and which parts by mathematical models.

simulated mechanical parts to the applied IM torque T_{im} and environmental forces F_{env}. Thus, its correct physical actuation is crucial to the EV emulation. This requirement is most naturally fulfilled by employing another electric drive that is connected to the same shaft with the induction machine and controlled for the correct shaft rotation speed.

As explained, the emulation platform outlined in figure 2.5 would allow emulating the Tazzari Zero drivetrain. Consequently, the on-road efficiency map method could be employed on it. The second requirement of the emulation platform is that it needs to be modifiable in order to accommodate the classic efficiency map protocol. This can be accomplished by modifying the control scheme of the system. In normal emulation, the IM torque instruction and the EIS electrical drive speed instruction are generated by the simulated part of the drivetrain and its control. In order to accommodate the classic protocol on the platform, these instructions could instead be directly determined so that desired operating points of the drivetrain would be reached. Therefore, the emulation platform of figure 2.5 fulfills all requirements of this work - it is capable of accommodating both the on-road efficiency map method and the classic protocol.

The tasks required for the implementation of the emulation platform will now be outlined. First, the Tazzari Zero drivetrain needs to be modeled mathematically. Second, the control algorithm for the drivetrain needs to be developed. Third, the implementation of the emulation interface system needs to be considered. In other words, an electrical variable-speed drive needs to be designed and implemented. Fourth, the emulation capability of the platform's practical implementation must be verified. Only then is it possible to proceed to the validation stage of the on-road method. Due to the complexity of the task, a structured approach would be beneficial. There are many interacting components to model and given the added layer of complexity due to the HIL simulation implementation, a clear view of the system is required. Furthermore, developing the control for this system would benefit from a systematic approach. Therefore, the next subsection introduces the methodology used in order to organise the mathematical model according to a set of rules and to develop the control of the system following a systematic procedure.

2.4 Control design using Energetic Macroscopic Representation

Given the complexity of the task, a structured approach would be beneficial to the organization of the mathematical model and to the control design. *Bond Graph* [29] is a well known approach to organize the model of a system according to a set of rules

and representing it graphically. Such visualization can yield insight into the structure and interrelations between subsystems and thus facilitate analysis. However, Bond Graph does not provide a systematic approach to developing the control of a system. In contrast, *Causal Ordering Graph (COG)* [30] yields the required control structure systematically from the COG representation of the model. However, COG is not well adapted to representing complex systems with multiple energy flows. A third methodology - *Energetic Macroscopic Representation (EMR)* [5, 31, 32] - has been developed on the basis of COG and also shares the useful quality of providing a systematic procedure for control design. In addition, EMR is particularly adapted to providing a macroscopic view of systems with complex, coupled energy flows and multiple energy sources. EMR has been used as a control design methdology and model organisation tool in various complex energy conversion applications such as hybrid electric vehicles [33, 34], fuel cell systems [35], wind energy systems [36] as well as subway [20] and locomotive applications [37]. Moreover, it has also proven to be useful in organizing HIL simulation systems [20, 36, 38]. EMR is employed in this work due to its proven suitability as a tool in the control design and model organisation of complex energy conversion systems.

The EMR procedure for model organization and control design is summarized in figure 2.6. The approach begins by organizing the model of the system according to EMR rules and representing it with EMR pictograms (orange rectangle in the figure). This then permits to systematically deduce the local control system (light blue trapezoid) by using the so called *Inversion-Based Control (IBC)* principle. At this stage, required measurements are given as part of the procedure and all system quantities
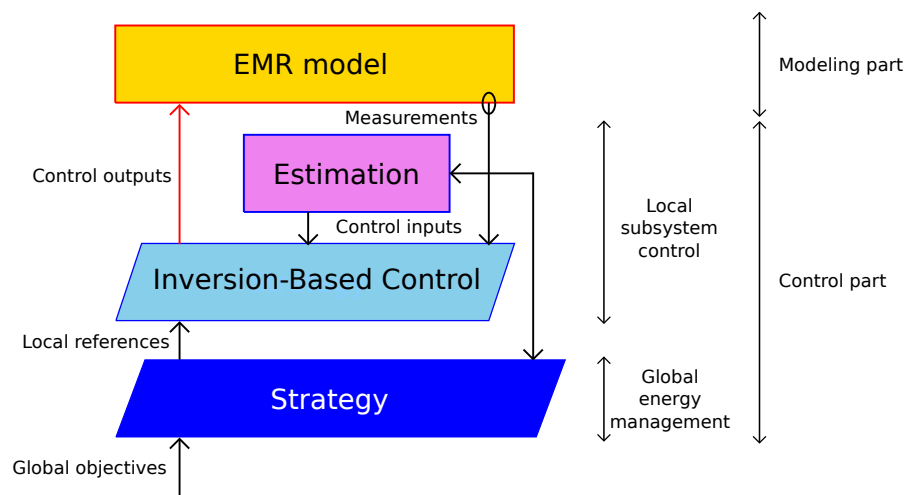

Figure 2.6: Control design using EMR.

are assumed measurable. As this is often not the case, impossible or unpractical measurements are subsequently replaced by estimations (purple rectangle). The local control level is responsible for the control of each respective subsystem. However, for the case of multiple energy flows, decisions also need to be made regarding the partition of these flows. This is done in the final control design step by determining the strategy level of the control (dark blue trapezoid). This means deciding how energy flows should be distributed and thus represents a higher-level energy management aspect of control. The remainder of this section is devoted to giving a more detailed description of this systematic EMR procedure to control design.

Step 1 - Organizing the system model according to EMR rules

The first step involves organizing the system model according to a set of EMR rules. Note thus that the actual modeling by mathematical equations or otherwise has to be performed before starting the control design procedure. This model is then organized to interconnected EMR elements according to the two following principles.

Interaction principle - The system is decomposed into basic subsystems in interaction. Each connection between two elements is done by a pair of exchange variables representing the action of one element and the other's reaction to it. The product of the action and reaction variables is the instantaneous power exchanged between the two elements.
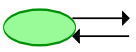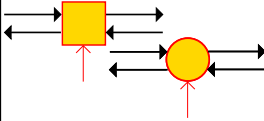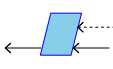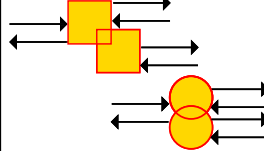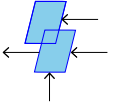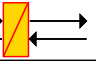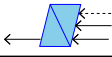
Causality principle - The only causality allowed by EMR is integral causality. This means that the output of a subsystem can either be an integral function of the input or have a rigid dependency on the input (no time dependency). However, the output of a subsystem may never be a derivative function of the input. This is because the time derivative of a function represents the instantaneous rate of change and thus requires knowledge of future evolutions. Such derivative causality is non-physical and not allowed by EMR.

Based on the interaction and causality principles, the model is organised into interacting EMR elements (orange and green pictograms), shown in table 2.1. Four basic types of EMR elements exist. Basic examples of these can be found in appendix B.

First, *source elements* are terminal elements that generate or receive energy to or from the rest of the system.

Second, *conversion elements* convert energy from one form to another without energy storage. Two types of conversion elements exist - monophysical and multiphysical. This indicates whether energy in converted within one physical domain (e.g. electric-electric) or between two different domains (e.g. electrical-mechanical). Conversion

Table 2.1: Elements of EMR and control.

	Source element (energy source)		
	Conversion element (energy conversion)		Direct inversion (open-loop control)
	Coupling element (energy distribution)		Direct inversion with distribution (open-loop control)
	Accumulation element (energy storage)		Indirect inversion (closed-loop control)

elements may have a tuning input[6] if the conversion is adjustable.

Third, *coupling elements* distribute energy between parts of the system without energy storage. As with conversion elements, distribution can be done within a single physical domain or between several domains.

Fourth, *accumulation elements* store energy while respecting the causality principle. In other words, the outputs of an accumulation element are always integral functions of the inputs.

After representing each part of the system with an EMR element, the elements are connected according to the interaction principle. The result is the EMR of the system (orange rectangle in figure 2.6). If direct connection of the elements is not possible (the input-output pairs of the elements are not complementary), certain *association rules* need to be used [5]. This situation is encountered in section 3.1 where its underlying reason is explained and resolved.

Step 2 - Defining the tuning path

Next, it is defined which system quantity should be controlled. Furthermore, it is decided which directly controllable variable (e.g. inverter switching functions) is chosen as the mechanism to act on the system. These choices are formalized by defining the so called *tuning path*. This is the path from the *tuning input* chosen to act on the system to the output variable that should be controlled.

Step 3 - Inversion of EMR elements on the tuning path

Next, focus is given to systematically obtaining a control structure for the system. This is done by following the principle of Inversion-Based Control. It states that the

---

[6]Power level variables are depicted by thick arrows while signal level variables such as tuning inputs and control signals are represented by thin, empty-headed arrows.

control of a given system is based on inverting the model of the system, as illustrated in figure 2.7. Suppose that the system output y should be controlled by creating the appropriate system input u. Given that the control input is the output reference y_{ref} then logically the control output u_{tun} must be formed as the inverse of the system model.
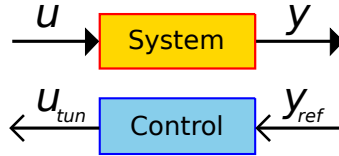

Figure 2.7: Inversion-Based Control principle.

Applied to the EMR of the system, the IBC principle requires inverting each of the EMR elements on the tuning path defined in step 2. Conversion and coupling elements can be inverted directly by reformulating the model equations. However, accumulation elements cannot be inverted in this way. This is because the output of an accumulation element is always an integral function of the input. Thus, direct inversion would mean that the control law for these subsystems would employ derivative functions on the control inputs. This is not allowed in EMR. Instead, an indirect inversion is performed by using a closed-loop controller (e.g. a PI-controller) and associated measurements. Closed-loop controller design principles used in this work are presented in appendix E. The appendix also shows the used controller parameter values. The IBC control elements corresponding to the different EMR elements are shown in table 2.1.

Step 4 - Estimations and simplifications

Inverting all the EMR elements on the tuning path yields the *Maximum Control Structure (MCS)* that is obtained without any subjective design choices. Up to this point, it has been assumed that all variables are measurable. As this is often not the case, impossible and impractical measurements need to be replaced by estimations (purple rectangle in figure 2.6). In order to obtain the required estimators, parts of the EMR system model can be reused. Furthermore, simplifications on the control structure can be made. For example, in the MCS all closed-loop controllers are designed with disturbance compensation. However, sometimes the compensation is impractical and can be removed at this stage in order to simplify the control. In this case, the corresponding closed-loop controller needs to reject the disturbance. Note that many choices made in this step are subjective, depending on the requirements and constraints of the actual implementation and on the system designer.

Step 5 - Defining strategy-level inputs

The local control level obtained in the previous steps is responsible for controlling each local subsystem in the optimal way. However, the inversions of coupling elements in step 3 lead to strategy-level inputs that determine how the different energy flows of the system should be partitioned. These are the strategy-level inputs that are defined in this final step of the control design procedure. They should in general be chosen so that the overall energy management of the system is optimized.

2.5 Conclusion

In this chapter, the goal of this Master's Thesis has been defined along with the approach taken to accomplish it. Section 2.1 introduced the context of the work, i.e. the larger scope of the research project. It was explained how obtaining a validated efficiency map static model for the Tazzari Zero would open various research possibilities. However, it was also established that this model cannot be obtained by conventional methods.

Section 2.2 then presented the on-road efficiency map method that could overcome these difficulties by obtaining an efficiency map based on measurements performed during a drive cycle. However, the method has not been experimentally validated. Consequently, this validation was defined as the goal of this Master's Thesis. The approach taken to the validation was then outlined. An emulation platform will be formed that is able to accommodate both the on-road efficiency map method and, with a slight modification, also the classic efficiency map protocol. Consequently, the on-road method could be validated if its resulting efficiency map had a high correspondance with the efficiency map obtained by the classic protocol.

In section 2.3, the implementation of the emulation platform was outlined. A HIL simulation implementation of the platform was chosen as a well-adapted approach, satisfying the main requirements of the platform. The HIL implementation was then outlined, dividing the drivetrain into physical and simulated parts as shown in figure 2.5. Moreover, it was established that an emulation interface system will also be needed to act between the physical and numeric domains. This interface system will include another electrical drive controlled for shaft rotation speed.

Due to the complexity of the design task, it was established that a clear view of the system is needed. Therefore, a structured approach to organizing the model of the system as well as designing its control would be beneficial. In section 2.4, it was shown how Energetic Macroscopic Representation provides these qualities. The EMR procedure to model organization and control design was then introduced. The

resulting general structure of the controlled system was shown in figure 2.6.

Chapter 3 will describe the detailed implementation of the emulation platform of figure 2.5. This includes the modeling of the system components and using the EMR procedure to organize the model and design its control. In addition, the correct performance of the emulation platform implementation will be verified before using it to validate the on-road efficiency map method. Once this verification has been completed, chapter 4 is then devoted to the validation of the on-road efficiency map method.

3 Emulation platform

As established in chapter 2, the on-road efficiency map method can be validated by comparing its result to an efficiency map obtained by the classic efficiency map protocol. This requires the emulation platform of figure 2.5 to be implemented. In addition, the platform's correct performance should be verified before using it for the validation. These are the goals of this chapter. The task can be divided into three parts. First, a control scheme is developped for the Tazzari Zero drivetrain shown in figure 2.2. Second, the emulation interface system shown in figure 2.5 is considered. These two subtasks correspond to the two first subsections of this chapter, 3.1 and 3.2, respectively. They lead to the theoretical implementation of the emulation platform. The third subsection 3.3 is devoted to verifying that the practical implementation of the platform has correct performance. This will then permit using the emulation platform as a tool to experimentally validate the on-road efficiency map method in chapter 4.

3.1 Inversion-Based Control of Tazzari Zero drivetrain

Forming the emulation platform is begun by considering the Tazzari Zero drivetrain and developing its control, i.e. ignoring the EIS for the moment. In order to utilize the IBC control design procedure, a model of the drivetrain is first required. Thus, the following considers the modeling of each of the drivetrain components.

Battery - The battery of the vehicle can be modeled by a simple constant voltage source. The corresponding EMR element is a source element as shown in the top left corner of figure 3.4 that shows the final EMR diagram of the Tazzari Zero drivetrain and its control. It has the battery voltage u_{bat} as the action variable and the current drawn by the inverter i_{inv} as the reaction variable.

Inverter - The three-phase Voltage-Source-Inverter (VSI) performs the function of converting the DC voltage of the battery into a set of three-phase voltages supplying the induction machine. It consists of six semiconductor switches[7] as shown in figure 3.1. However, the two switches of each commutation cell connected to one machine terminal need to be controlled complementarily to avoid shorting or disconnecting the respective machine terminal from the battery. For example, if the leftmost upper switch has its switching order s_{11} set to the conducting state, the leftmost lower switch should have its switching order s_{12} set to the non-conducting state.

---

[7]Each semiconductor switch consists of a transistor-diode pair to allow current flow in both directions.
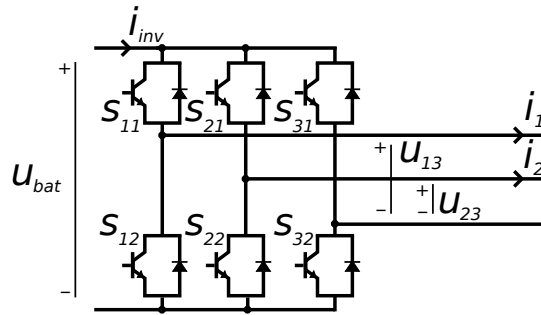
Figure 3.1: Voltage-Source-Inverter.

Only two of the AC side line-to-line voltages are independent and thus the output of the inverter can be given as a 2x1 vector $\underline{u}_{inv}$. Defining each semiconductor switch to have value 1 in the conducting state and value -1 in the non-conducting state, the AC side voltage output can be written as given in equation [(3)-1] with $\underline{m}$ defined as the modulation function of the VSI[8]. The battery side current i_{inv} is obtained from the machine terminal currents [9] according to the lower equation of [(3)-1]. Here, η_{inv} is the inverter efficiency and the direction of positive power flow $P \geq 0$ is defined as being from the battery to the rest of the system.

$$\begin{cases} \underline{u}_{inv} = \begin{bmatrix} u_{13} \\ u_{23} \end{bmatrix} = \frac{1}{2} \begin{bmatrix} s_{11} - s_{31} \\ s_{21} - s_{31} \end{bmatrix} u_{bat} = \underline{m} u_{bat} \\ \\ i_{inv} = \underline{m} \bullet \begin{bmatrix} i_1 \\ i_2 \end{bmatrix} \frac{1}{\eta_{inv}^k} = \frac{\underline{m} \bullet \underline{i}_{im}}{\eta_{inv}^k}, \quad k = \begin{cases} 1 & \text{if } P \geq 0 \\ -1 & \text{if } P < 0 \end{cases} \end{cases} \qquad \text{[(3)-1]}$$

Equation [(3)-1] is represented by a monophysical EMR conversion element with the modulation function $\underline{m}$ as the tuning input. It is shown in the EMR diagram of figure 3.4.

Transformations - The well-known AC machine *vector control* principle [39] will be used in this work as the working principle of the electrical drive control. This involves using a machine model with space vectors in the rotating *dq coordinate system*. Two operations are needed to construct a space vector representation from the

---

[8]Modulation function $\underline{m}$ represents how the inverter switching is controlled. However, in practical control of a physical inverter, the modulation function is not directly usable for various reasons. These aspects are covered in appendix G.

[9]Current $\underline{i}_{im}$ represents the currents going into the machine terminals, i.e. the currents of the inverter lines on the AC side. Note that for a delta connection these currents are not equal to machine phase currents. The machine connection type is considered in the **Transformations** subsection.

inverter line-to-line voltages. First, the voltages over individual machine phases need to be deduced from the VSI line-to-line voltages. This is accomplished with the matrix operator $[T_{uv}]$ in equation [(3)-2]. Its contents depend on whether the machine is connected in star or in delta. The derivation of these matrices is shown in appendix D. Second, the voltage space vector needs to be constructed from the machine phase voltages and transformed into the dq coordinate system. This is described by the well-known *Park transformation* operator $\left[T(\theta_{d/s})_{PARK}\right]$ in equation [(3)-2]. Here $\theta_{d/s}$ is the transformation angle characterizing the dq coordinate system. The Park transformation derivation is shown in appendix D.

$$\underline{v}_{s,dq} = \left[T(\theta_{d/s})_{PARK}\right] [T_{uv}] \, \underline{u}_{inv} \qquad \text{[(3)-2]}$$

Conversely, the machine terminal currents are obtained from the machine current dq space vector by performing *the inverse Park transformation* with $\left[T(\theta_{d/s})_{PARK}\right]^{-1}$ and then using matrix operator $[T_{ii}]$ to obtain the inverter line currents from the machine phase currents.

$$\underline{i}_{im} = [T_{ii}] \left[T(\theta_{d/s})_{PARK}\right]^{-1} \underline{i}_{s,dq} \qquad \text{[(3)-3]}$$

These two equations are represented by an EMR monophysical conversion element with a supplementary input of the dq transformation angle $\theta_{d/s}$. This is shown in figure 3.4.

It is important for the machine modeling to well define the different space vector coordinate systems used. Three such systems - shown in figure 3.2 - exist with relevance to the modeling task.
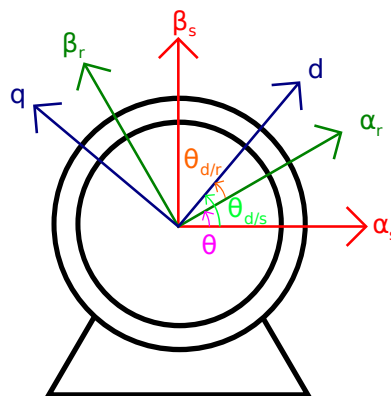

Figure 3.2: Coordinate systems and related transformation angles.

First, there is the *stator coordinate system* denoted by the axes α_s and β_s, respectively. A stator coordinate representation results from using only the space vector definition without any further coordinate transformations, i.e. the Park transformation with zero angle. This corresponds to a space vector representation in a coordinate system fixed to the stator of the machine. Second, there is the *rotor coordinate system* denoted by the axes α_r and β_r. This coordinate system expresses space vectors in a coordinate system rotating at the rotor electrical angular frequency ω as given by equation

$$\omega = p\Omega_{sh} \qquad \text{[(3)-4]}$$

where p is the pole pair number of the machine and Ω_{sh} the shaft angular frequency. Finally, the *dq coordinate system* is denoted by the d and q axes. It enables observing the space vectors in a coordinate system that rotates with the flux of the machine. The angle $\theta_{d/s}$ defining the dq coordinate system is given by

$$\theta_{d/s} = \theta + \theta_{d/r} \qquad \text{[(3)-5]}$$

Induction machine - Next, the actual induction machine operation is considered. The basic voltage and flux equations of a squirrel cage induction machine are[10]

$$\underline{v}_{s,\alpha_s\beta_s} = R_s\underline{i}_{s,\alpha_s\beta_s} + \frac{d\underline{\Phi}_{s,\alpha_s\beta_s}}{dt} \qquad \text{[(3)-6]}$$

$$\underline{\Phi}_{s,\alpha_s\beta_s} = L_s\underline{i}_{s,\alpha_s\beta_s} + M_{sr}\underline{i}_{r,\alpha_s\beta_s} \qquad \text{[(3)-7]}$$

$$\underline{v}_{r,\alpha_r\beta_r} = 0 = R_r\underline{i}_{r,\alpha_r\beta_r} + \frac{d\underline{\Phi}_{r,\alpha_r\beta_r}}{dt} \qquad \text{[(3)-8]}$$

$$\underline{\Phi}_{r,\alpha_r\beta_r} = L_r\underline{i}_{r,\alpha_r\beta_r} + M_{sr}\underline{i}_{s,\alpha_r\beta_r} \qquad \text{[(3)-9]}$$

These are transformed into dq coordinates. The resulting equations can be simplified by assuming so called *rotor field orientation*. This signifies that the d axis of the coordinate system is in the direction of the rotor flux. Combining rotor field orientation with separating the real and imaginary parts of the equations leads to the simplified group of eight equations

---

[10]Equations [(3)-6]-[(3)-9] describe dynamic IM operation but without taking into account non-linear phenomena in the machine. Such phenomena are *saturation* and *magnetic hysteresis* of the machine iron as well as the *skin effect* in conductors and temperature dependance of parameters. These simplifications allow considering the inductances and resistances of the machine to remain constant.

$$\begin{cases} v_{sd} = R_s i_{sd} + \dfrac{d\Phi_{sd}}{dt} - \omega_{d/s}\Phi_{sq} \\[2mm] v_{sq} = R_s i_{sq} + \dfrac{d\Phi_{sq}}{dt} + \omega_{d/s}\Phi_{sd} \\[2mm] v_{rd} = 0 = R_r i_{rd} + \dfrac{d\Phi_{rd}}{dt} \\[2mm] v_{rq} = 0 = R_r i_{rq} + \omega_{d/r}\Phi_{rd} \end{cases} \qquad [(3)\text{-}10]$$

$$\begin{cases} \Phi_{sd} = L_s i_{sd} + M_{sr} i_{rd} \\[2mm] \Phi_{sq} = L_s i_{sq} + M_{sr} i_{rq} \\[2mm] \Phi_{rd} = L_r i_{rd} + M_{sr} i_{sd} \\[2mm] \Phi_{rq} = 0 = L_r i_{rq} + M_{sr} i_{sq} \end{cases} \qquad [(3)\text{-}11]$$

In these equations, the angular frequency $\omega_{d/r}$ is the rate of change of the transformation angle $\theta_{d/r}$ in figure 3.2 and it corresponds to the relative rotation of the dq coordinate system with respect to the rotor coordinate system. The dependencies between the angular frequencies of the different coordinate systems are described by

$$\omega_{d/s} = \omega + \omega_{d/r} \qquad [(3)\text{-}12]$$

Equations [(3)-10] and [(3)-11] can be rewritten with the stator currents as state variables. By utilizing the Laplace transform with Laplace variable s, the stator currents can be written as transfer functions

$$\begin{cases} i_{sd} = \dfrac{K_s}{1 + s\sigma\tau_s}(v_{sd} - e_{sd}), \\[3mm] i_{sq} = \dfrac{K_s}{1 + s\sigma\tau_s}(v_{sq} - e_{sq}) \end{cases} \qquad [(3)\text{-}13]$$

with the *back emf's* of the machine given by

$$\begin{cases} e_{sd} = -\dfrac{M_{sr}}{\tau_r L_r}\Phi_{rd} + \dfrac{M_{sr}^2}{\tau_r L_r}i_{sd} - \omega_{d/s}\sigma L_s i_{sq} \\[3mm] e_{sq} = \omega_{d/s}\sigma L_s i_{sd} + \omega_{d/s}\dfrac{M_{sr}}{L_r}\Phi_{rd} \end{cases} \qquad [(3)\text{-}14]$$

Above the IM winding static gain K_s, stator time constant τ_s, rotor time constant τ_r and *leakage factor* σ are defined as

$$K_s = \frac{1}{R_s}, \quad \tau_s = \frac{L_s}{R_s}, \quad \tau_r = \frac{L_r}{R_r}, \quad \sigma = 1 - \frac{M_{sr}^2}{L_s L_r} \qquad \text{[(3)-15]}$$

Finding the torque expression for the induction machine requires finding the active electrical power that is converted into mechanical power. This occurs in the rotor circuit as described by equations [(3)-8] and [(3)-9]. Expressing these equations in stator coordinates yields the power converted from electrical to mechanical as the interaction of the rotor current and voltage $-j\omega \underline{\Phi}_{r,\alpha_s\beta_s}$. This voltage is developed by the machine in the rotor circuit as a reaction to the mechanical rotation. Obtaining the converted power according to [(D)-6] and comparing it to the mechanical rotational power yields the torque of the induction machine as

$$T_{im} = p\frac{M_{sr}}{L_r}\Phi_{rd}i_{sq} \qquad \text{[(3)-16]}$$

The torque is seen to depend only on the stator current q component. The rotor flux of the machine is obtained from equations [(3)-10] and [(3)-11] as transfer function

$$\Phi_{rd} = \frac{M_{sr}}{s\tau_r + 1}i_{sd} \qquad \text{[(3)-17]}$$

Thus, the rotor flux and torque control can be separated by the respective control of stator current d and q components. The machine model is finalized by considering the dq coordinate system transformation angle $\theta_{d/s}$ that is obtained as the integral of the stator angular frequency $\omega_{d/s}$. This is given by equations [(3)-4], [(3)-10], [(3)-11] and [(3)-12] as

$$\theta_{d/s} = \int \omega_{d/s}\, \mathrm{d}t = \int \left(p\Omega_{sh} + \frac{M_{sr}}{\tau_r}\frac{i_{sq}}{\Phi_{rd}} \right) \mathrm{d}t \qquad \text{[(3)-18]}$$

The induction machine model is represented by three EMR elements as shown in figure 3.4. First, the voltage-current conversion described by equation [(3)-13] is represented by an accumulation element due to the temporal nature of these equations. Second, the electromechanical conversion given by the torque equation [(3)-16] and the back emf equation [(3)-14] are represented by a multiphysical coupling element. This element also supplies the Park transformation angle to the EMR transformation element according to equation [(3)-18]. Third, the rotor flux dynamics given by equation [(3)-17] must be represented by another accumulation element due to the relation's temporal nature. These three elements can be seen in the EMR diagram of

figure 3.4.

Shaft - The shaft of the machine is described by the rotational movement law

$$J\frac{d\Omega_{sh}}{dt} = T_{im} - T_{res} - f\Omega_{sh} \qquad \text{[(3)-19]}$$

where J and f are the moment of inertia and the friction coefficient of the shaft and T_{res} the resistive torque corresponding to environmental forces. This temporal relation is represented by an accumulation element. This element and other EMR elements formed below for the remaining mechanical parts of the drivetrain are not directly visible in the EMR diagram of figure 3.4. This is because connecting these EMR elements requires the use of EMR association rules [5]. This is dealt with below in step 1 of the IBC procedure and will result in the EMR diagram of figure 3.4.

Single ratio gearbox - Since electrical machines can be operated with high efficiency over wide ranges of speed and torque values, a multi-ratio gearbox is not necessary. However, since typically the electrical machine base speed is higher than typical desired vehicle wheel rotation speeds, a single-ratio gearbox is used. The speed-torque conversion is described by equations

$$\begin{cases} \Omega_{sh} = k_{gear}\Omega_{diff} \\ T_{gear} = k_{gear}\eta_{gear}^{k}T_{res} \end{cases} \qquad \text{[(3)-20]}$$

with k_{gear} the speed reduction ratio, Ω_{diff} the reduced rotation speed and T_{gear} the torque on the differential side with η_{gear} the efficiency of the gearbox. These relations are represented by an EMR monophysical conversion element.

Differential and wheels - The mechanical differential compensates the different rotation speeds of the wheels during cornering. As the goal of this work relates to the energetic performance of the drivetrain and the effect of the differential during cornering is minor in terms of overall efficiency, the turning of the wheels is neglected. This allows to consider the differential only in terms of its reduction of rotation speed, yielding an equation equivalent to [(3)-20]. Furthermore, as no cornering is considered, the two wheels of the vehicle can be replaced with one equivalent wheel that converts rotational movement to linear movement. Consequently, the differential and wheels are modeled by equations

$$\begin{cases} \Omega_{diff} = k_{diff}\dfrac{v_{veh}}{r_{wh}} \\ F'_{dt} = \dfrac{k_{diff}\eta_{diff}^{k}T_{gear}}{r_{wh}} \end{cases} \qquad \text{[(3)-21]}$$

with k_{diff} the speed reduction ratio of the differential, F'_{dt} the traction force generated by the drivetrain[11], η_{diff} the efficiency of the differential and r_{wh} the wheel radius. These relations are represented by an EMR monophysical conversion element.

Mechanical brake - The mechanical brake transforms kinetic energy into heat and is represented by a controlled EMR source element with generated braking force F_b and braking force reference $F_{b,ref}$. These are assumed equal, i.e. the desired mechanical braking force can always be produced. The braking force is then added to the traction force generated by the drivetrain to obtain total propulsion force F'_{tract}. This is given by

$$F'_{tract} = F'_{dt} + F_b \qquad \text{[(3)-22]}$$

This coupling of forces is represented by a monophysical EMR coupling element.

Chassis - The chassis of the vehicle has already been modeled by equation [(2)-3] except that here strictly the vehicle mass m is considered as movement inertia. The temporal relationship is represented by an EMR accumulation element.

Environment - The environment has already been modeled in equation [(2)-4] and it is represented by an EMR source element with the vehicle speed v_{veh} as input and the resistive forces F_{env} as output.

All components of the drivetrain have now been modeled while already initially considering the respective EMR elements. Thus, the actual Inversion-Based Control design procedure can now be begun in order to obtain the control structure for the system.

Step 1 - Organizing the system model according to EMR rules - When attempting to connect the EMR elements, it becomes apparent that the input-output pairs are not complementary and consequently the elements cannot be directly connected. This is depicted in figure 3.3. Here, this so called *conflict of association* is due to the accumulation elements of the shaft and the chassis imposing separately the shaft rotational speed and the vehicle speed. However, in reality these two speeds are related by a rigid dependency. In other words, there is in reality only one state variable for the speed, not two.

The issue is overcome by utilizing the so called *association rules*. First, the *permutation rule* allows swapping the places of two EMR elements on the condition that they impose the same global outputs from the same global inputs [5]. This permits moving

---

[11]Primed notation is used at this stage for the drivetrain and traction forces F'_{dt} and F'_{tract} because the unprimed notation is reserved for the corresponding final equations [(3)-23] and [(3)-24].
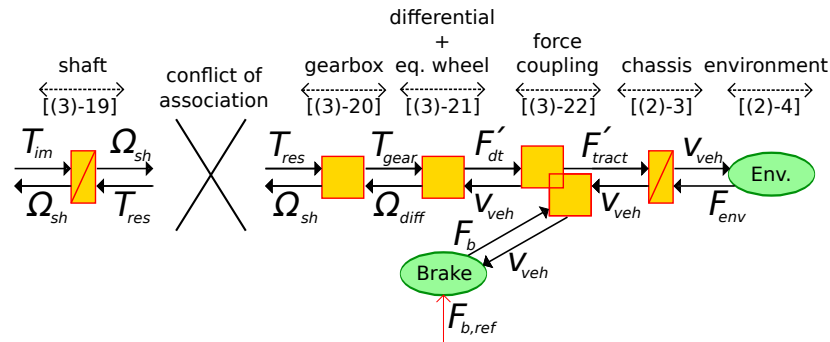
Figure 3.3: Conflict of association when connecting the EMR elements.

the shaft accumulation element next to the chassis accumulation element. Then, the *merging rule* is used to combine the two accumulation elements into one equivalent accumulation element. This is done simply by combining the model equations of the two elements. After this, all the EMR elements can be connected since the input-output pairs are complementary. The merged shaft and chassis are then described by

$$M_{tot}\frac{d}{dt}v_{veh} = F_{tract} - F_{env} - B_{tot}v_{veh}$$

$$\text{where} \quad \begin{cases} M_{tot} &= \frac{(k_{diff}k_{gear})^2(\eta_{diff}\eta_{gear})^k J}{r_{wh}^2} + m \\ B_{tot} &= \frac{(k_{diff}k_{gear})^2(\eta_{diff}\eta_{gear})^k f}{r_{wh}^2} \end{cases} \qquad \text{[(3)-23]}$$

In addition, the conversion elements of the gearbox, the differential and the equivalent wheel are merged to obtain a simplified EMR diagram. The merged gearbox, differential and equivalent wheel are then described by

$$\begin{cases} F_{dt} &= \frac{k_{diff}k_{gear}(\eta_{diff}\eta_{gear})^k}{r_{wh}}T_{im} \\ \Omega_{sh} &= \frac{k_{diff}k_{gear}}{r_{wh}}v_{veh} \end{cases} \qquad \text{[(3)-24]}$$

This leads to the final EMR diagram of the Tazzari Zero drivetrain shown in figure 3.4 by the orange and green EMR elements.

Step 2 - Defining the tuning path - Next, the tuning path is defined from the tuning input chosen to act on the system to the output variable to control. The suitable tuning input is clearly the modulation function of the inverter while the output to
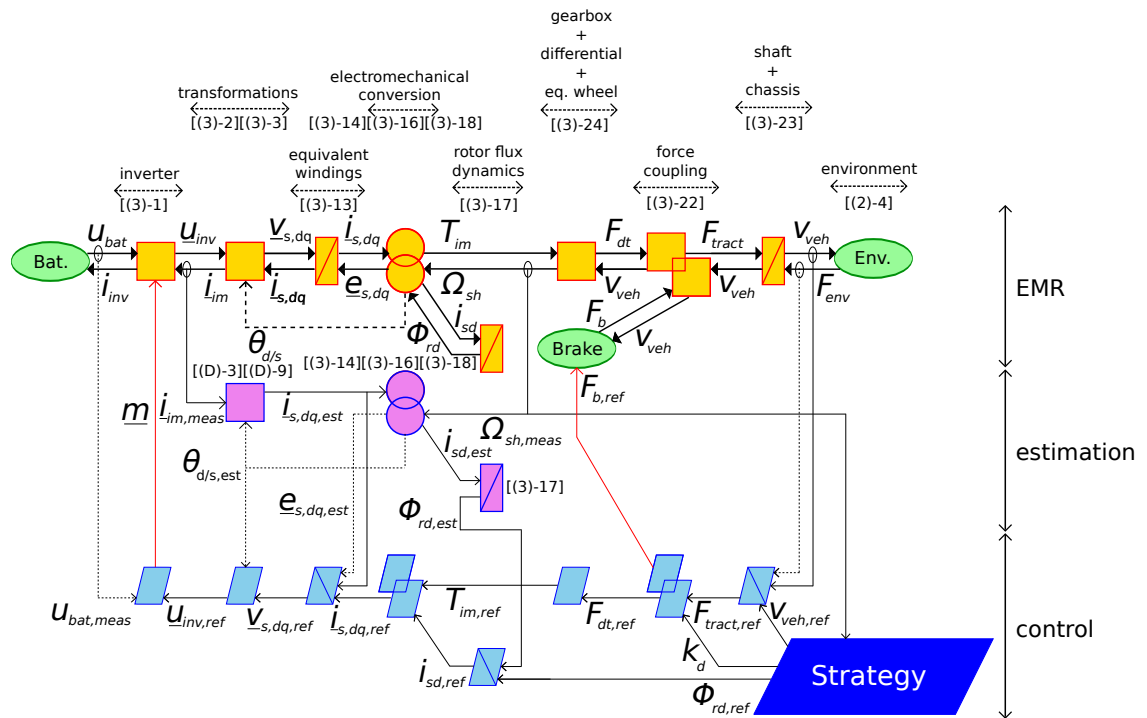
Figure 3.4: Tazzari Zero drivetrain and its control structure.

control is the vehicle speed[12]. The tuning path is depicted below in figure 3.5.
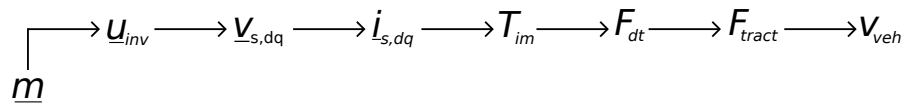

Figure 3.5: Tuning path of the Tazzari Zero drivetrain.

Step 3 - Inversion of EMR elements on the tuning path - With the model represented by means of the EMR diagram, the development of the control structure is straightforward. Each EMR element is inverted by a corresponding control element according to the principles given in section 2.4. The control element that warrants extra attention is the inversion of the braking and drivetrain force coupling element. This corresponds to the partition of braking force into mechanical braking and regenerative braking using the electrical machine. Using the distribution parameter k_d, the braking force reference $F_{tract,ref}$ can be defined as

---

[12]Note that in the presence of a human driver the controlled output variable is torque with the driver giving the control instruction by using the accelerator. The driver's desired vehicle speed is then reached by the driver himself acting as a closed-loop speed controller. However, as in the final emulation setup there will be no driver and the speed cycle of the vehicle is defined in advance, a speed controller is needed to replace the accelerator actions of the driver.

$$\begin{cases} F_{dt,ref} & = k_d F_{tract,ref} \\ F_{b,ref} & = (1 - k_d) F_{tract,ref} \end{cases} \qquad \text{[(3)-25]}$$

For an actual EV, it would obviously be beneficial to maximize regenerative braking and to minimize mechanical braking. However, the regenerative braking capacity is limited by the maximum currents of the electrical machine and in particular the battery's ability to accept high recharging currents. In addition, regenerative braking is possible only with two wheels because the Tazzari Zero traction drive is connected to only one axle. Indeed, based on actual Tazzari Zero battery measurements, regenerative braking is very limited and thus in this work it is assumed that all braking is done with the mechanical brake[13].

This step yields the light blue control elements shown in figure 3.4. The result of this design step is the MCS that assumes all system variables are directly measurable. Three closed-loop controllers are required for the respective control of the vehicle speed, rotor flux and stator currents[14]. The design of these controllers along with all the other closed-loop controllers that will later be introduced, is explained in appendix E.

Step 4 - Estimations and simplifications - Several measurements of the MCS of the system are not directly realizable. Thus, the purple estimation blocks of figure 3.4 are introduced in this step by reusing the model equations. First, the flux controller's flux level control input can be estimated with equation [(3)-17]. Second, the stator current controller needs the stator dq currents which can be obtained by measuring two inverter line currents i_1 and i_2 and then forming the dq current estimate with equations [(D)-3] and [(D)-9]. This estimation and the inversion of the EMR transformation element needs the dq coordinate system angle that can be estimated with [(3)-18]. Finally, the back emf's used in the disturbance compensation of the stator current controller can be estimated according to equation [(3)-14].

Step 5 - Defining strategy-level inputs - Three strategy-level inputs need to be defined. First, the vehicle reference speed $v_{veh,ref}$ is defined by the drive cycle. Second, the braking distribution parameter k_d is set to zero for negative traction forces (mechanical braking only) and to 1 for positive traction forces (acceleration using mechanical brake is not possible). Third, the rotor flux reference value is set either to the nominal value at low speeds or decreased at high speeds. This is determined by

---

[13]This is of no practical significance in terms of the goal of this work since in the on-road efficiency map method the braking phases are ignored in any case.

[14]Since the stator currents are given by the two-dimensional quantity $\underline{i}_{s,dq}$, two scalar-valued closed-loop controllers are needed for stator current control.

the flux weakening strategy covered in appendix F.

3.2 Emulation interface system

The main difference of the controlled emulation platform with regards to the controlled Tazzari drivetrain is the presence of the emulation interface system. As explained in section 2.3, this system must convert the physical induction machine torque T_{im} into numerical information and to physically actuate the machine shaft speed Ω_{sh} calculated by the simulation part.

The numerical value of the IM torque can be obtained simply by reusing the model equation [(3)-16] to obtain an estimation. The shaft speed actuation is most naturally done by employing a second electrical drive coupled to the same shaft as the induction machine. Due to practical availability of machines in the laboratory of L2EP, this second machine is a permanent magnet synchronous machine (PMSM) with salient poles. Thus, the task at hand is the design of a PMSM shaft speed drive. This drive consists of the PMSM supplied by a dedicated inverter and a DC bus. Section 3.1 can be utilized for the modeling of the inverter, DC bus (modeled as a voltage source like the battery) and transformations. Therefore, only the PMSM needs to be modeled before starting the IBC control design procedure.

Permanent magnet synchronous machine - The main difference compared to an induction machine is that the rotor electrical angular frequency ω is the same as the stator angular frequency $\omega_{d/s}$, i.e.

$$\omega_{d/s} = \omega = p\Omega_{sh} \qquad [(3)\text{-}26]$$

The basic voltage and flux equations of a PMSM with salient poles are

$$\underline{v}_{s,\alpha_s\beta_s} = R_s\underline{i}_{s,\alpha_s\beta_s} + \frac{d\underline{\Phi}_{s,\alpha_s\beta_s}}{dt} \qquad [(3)\text{-}27]$$

$$\Phi_{sd} = L_d i_{sd} + \Phi_{pm} \qquad [(3)\text{-}28]$$

$$\Phi_{sq} = L_q i_{sq} \qquad [(3)\text{-}29]$$

The synchronization allows writing the flux equations directly in the synchronous dq coordinate system. First, rotor field orientation is done by defining the d axis to be in the direction of the permanent magnet flux Φ_{pm} crossing the airgap. The components of the stator flux - described by equations [(3)-28] and [(3)-29] - consist of the stator current magnetization via inductances L_d and L_q as well as the permanent magnet

flux in the d direction[15]. The stator voltage equation [(3)-27] can be transformed into dq coordinates, yielding the d and q components as

$$\begin{cases} v_{sd} = R_s i_{sd} + \dfrac{d\Phi_{sd}}{dt} - \omega\Phi_{sq} \\[2mm] v_{sq} = R_s i_{sq} + \dfrac{d\Phi_{sq}}{dt} + \omega\Phi_{sd} \end{cases} \qquad \text{[(3)-30]}$$

Solving the PMSM equations for stator currents and Laplace-transforming yields

$$\begin{cases} i_{sd} = \dfrac{K_{sm}}{s\tau_d + 1}(v_{sd} - e_{sd}) & \text{where} \quad K_{sm} = \dfrac{1}{R_s}, \quad \tau_d = \dfrac{L_d}{R_s} \\[3mm] i_{sq} = \dfrac{K_{sm}}{s\tau_q + 1}(v_{sq} - e_{sq}) & \text{where} \quad \tau_q = \dfrac{L_q}{R_s} \end{cases} \qquad \text{[(3)-31]}$$

with the back emf's of the machine given as

$$\begin{cases} e_{sd} = -\omega L_q i_{sq} \\[2mm] e_{sq} = \omega(L_d i_{sd} + \Phi_{pm}) \end{cases} \qquad \text{[(3)-32]}$$

The electrical active power that is converted into mechanical power corresponds to the interaction of the back emf's and the stator currents. Obtaining this power according to [(D)-6] and comparing it to the mechanical rotational power yields the torque of the PMSM as

$$T_{sm} = ((L_d - L_q)i_{sd}i_{sq} + \Phi_{pm}i_{sq})p \qquad \text{[(3)-33]}$$

The PMSM model is represented by two EMR elements. First, the voltage-current conversion described by expression [(3)-31] is represented by an accumulation element due to the temporal nature of these equations. Second, the electromechanical conversion given by the torque equation [(3)-33] and the back emf equations of [(3)-32] are represented by a multiphysical conversion element. This element also supplies the Park transformation angle to the transformation element. Having modeled the PMSM, the IBC design procedure can now be used to form the PMSM drive's speed control.

Step 1 - Organizing the system model according to EMR rules - The structure of the PMSM drive is almost identical to that of the Tazzari Zero drivetrain's electrical part except that the machine type has been changed and the battery has been replaced by a DC bus. The corresponding EMR elements can be connected directly

---

[15]Saliency of the machine rotor indicates that the inductances in the d and q directions are not equal.

without the use of permutation and merging rules. This leads to the orange and green elements shown on the top right of the EMR diagram of figure 3.7 that shows the final EMR representation of the emulation platform[16].

Step 2 - Defining the tuning path - The tuning path of the PMSM drive is from the modulation function tuning input of the inverter to the shaft rotation speed output of the shaft. This is illustrated in figure 3.6.

$$\Omega_{sh} \longleftarrow T_{sm} \longleftarrow \underline{i}_{sm,dq} \longleftarrow \underline{v}_{sm,s,dq} \longleftarrow \underline{u}_{sm,inv} \longleftarrow$$
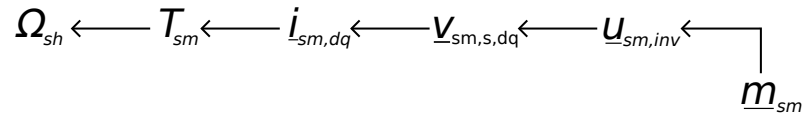$$\underline{m}_{sm}$$

Figure 3.6: Tuning path of the emulation interface system, i.e. the PMSM speed drive.

Step 3 - Inversion of EMR elements on the tuning path - Each EMR element on the tuning path is next inverted by a corresponding control element. Two closed-loop controllers result, one for the inversion of stator current dynamics and one for the inversion of the mechanical dynamics of the shaft. Furthermore, an inversion of the coupling element is present, defining how the stator currents $i_{sm,sd}$ and $i_{sm,sq}$ are determined so that the torque instruction $T_{sm,ref}$ is realized. As shown by the torque equation [(3)-33], unless the saliency of the rotor is very high, the torque is mostly produced by the current q component while higher d current levels are used only in field weakening operation. Thus, the stator current d component is considered a strategy-level input with the q component then determined based on the torque equation.

Step 4 - Estimations and simplifications - The estimations needed for the PMSM are very similar to those of the induction machine. The machine connection type matrix [(D)-3] and Park transformation [(D)-9] are used to estimate $\underline{i}_{sm,dq}$ from the synchronous machine terminal currents. Note that for the synchronous machine, the dq coordinate system angle corresponds directly to the physical rotor position. Therefore, the transformation angle θ_{sm} can be directly measured instead of being estimated from the shaft speed measurement[17]. Usually a direct measurement[18] is

---

[16]When the two machines are considered together and there is a risk of confusion, 'sm' is added to the subindices of synchronous machine quantities.

[17]This is not possible for the induction machine because the rotor flux rotates with respect to the rotor.

[18]Typically, a *tachometer* is used for position measurement which in fact is rather a measure of how much the rotor has rotated since the beginning of control than the actual rotor position. For this reason, before starting control it is useful to initialize the rotor to a known position by applying fixed inverter switch positions that generate a stator flux in a known direction. The rotor then aligns itself so that the rotor's permanent magnet flux is in the same direction. In this way, the control can be started with

preferrable to estimating the position from rotation speed as even small offsets in the speed measurement lead to bad estimations of the rotor position and possible loss of control. Other estimations used are the back emf equations of [(3)-32] for disturbance compensation in the stator current controllers, as well as the use of the induction machine torque estimate for disturbance compensation in the inversion block of the shaft.

Step 5 - Defining strategy-level inputs - The only strategy-level input for the PMSM drive is the stator current d component reference. As the saliency of the laboratory's PMSM (see appendix C) is rather small, the torque-producing capability of $i_{sm,sd}$ is negligable compared to $i_{sm,sq}$. Thus, the d component is simply set to zero in order to reduce the RMS value of the stator currents[19], thereby reducing also the stator copper losses. Moreover, field-weakening that would require high d current levels of the PMSM is avoided by utilizing a DC bus level that is sufficient to reach desired rotation speeds.

EMR diagram of emulation platform - All the previous results may now be collected to form the final EMR representation of the emulation platform, shown below in figure 3.7. This is done by considering how figure 2.5 translates to an EMR representation. First, the EMR diagram of the Tazzari Zero drivetrain as shown in figure 3.4 is modified for the purposes of the emulation platform. This means that the mechanical part of the drivetrain is implemented by the mathematical models and not by physical components. Thus, these EMR elements have been colored purple. The drivetrain control scheme remains unchanged. The EMR diagram of the emulation platform is then completed by adding the emulation interface system, i.e. the PMSM speed drive to the system. As explained, the EIS needs to physically actuate the shaft speed response of the simulated part. The numeric IM torque value needed by the simulated part can be estimated by the torque expression [(3)-16].

It is seen that both the torque instruction of the IM and the speed instruction of the PMSM are generated by the simulated part and its control. The shaft speed instruction of the PMSM corresponds to the vehicle's linear speed. It is thus defined by the drive cycle $v_{veh,ref}$ and the ability of the simulated part's control to follow this reference. The IM torque instruction is generated as the tractive torque that is needed to overcome the imposed environmental conditions. Consequently, higher IM torque instructions are generated if the imposed environmental conditions are more

---

a known rotor position.

[19]For a non-salient rotor, a zero d direction stator current results in maximum torque for a given RMS value of the stator currents, as can be seen from equation [(3)-33]. For the PMSM of the laboratory with low saliency, the simplicity of setting the d current to zero is deemed a greater advantage than the very small improvement in torque production capability when the optimal current space vector $\underline{i}_{sm,dq}$ with a small d component is computed.

resistive, e.g. the entire drive cycle is uphill.

Figure 3.7: Emulation platform and its control structure.

Reduced power emulation platform - One more consideration needs to be taken into account before the performance of the implemented emulation platform can be verified. This relates to the relation of power levels of the emulation platform and of the Tazzari Zero. As described in appendix C, the power level that can be used with the practical implementation of the emulation platform is limited. This is due to the way the electrical power is supplied to the two electrical drives of the setup and equipment limitations. Consequently, the power level of the emulation platform needs to be adapted for the physical equipment of the setup.

The power level adaptation is done so that the simulated part operates at the full power level while the physical equipment operates at reduced power [5]. Thus, two

power level adaptation blocks are added to the EMR diagram. The first is inserted between the simulated part of the drivetrain and the physical equipment of the setup (EIS and physical part of drivetrain). The second is placed between the two power levels used in the control of the drivetrain. The resulting EMR diagram is shown below in figure 3.8.
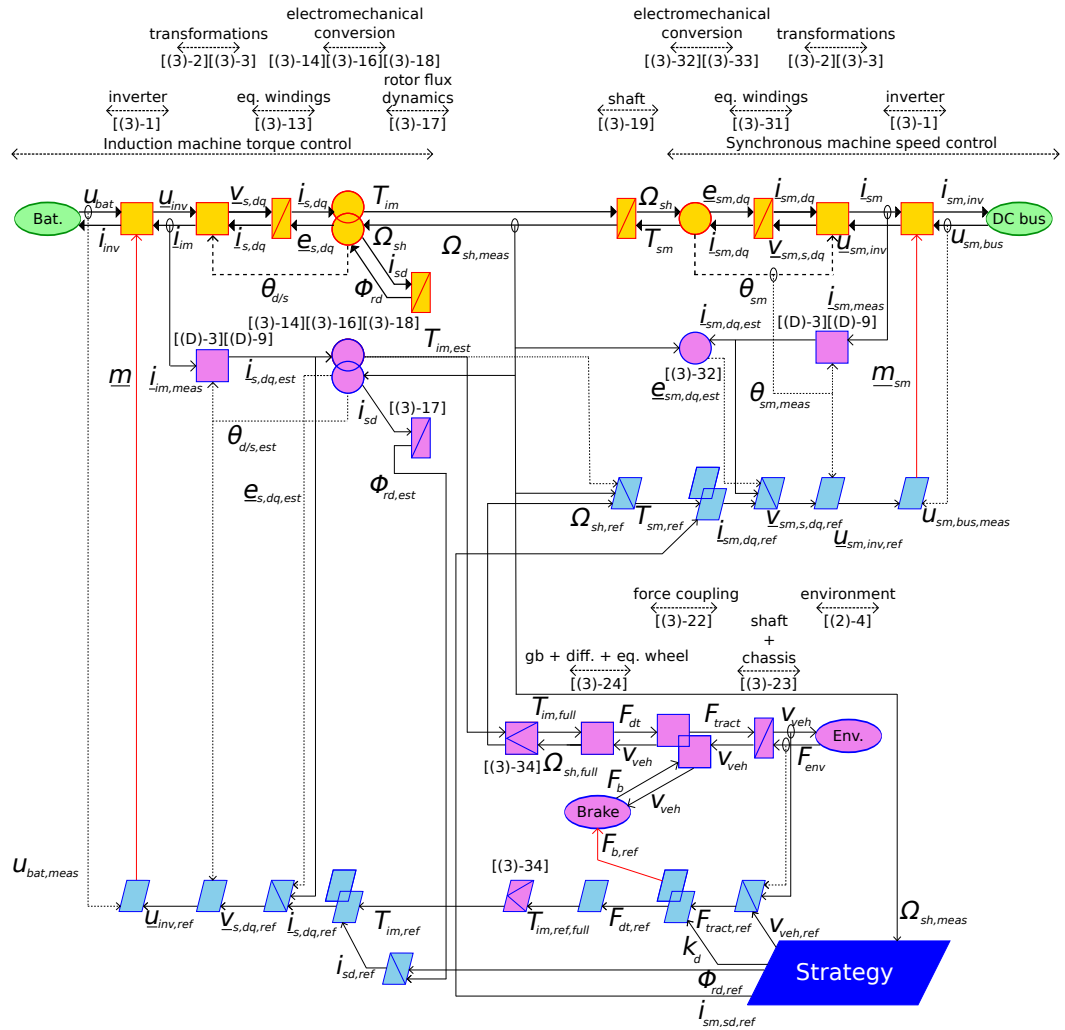
Figure 3.8: Reduced power implementation of the emulation platform.

The adaptation blocks modify the power level linearly according to

$$
\begin{cases}
T_{im,full} = T_{im,est} a_T \\
T_{im,ref} = \dfrac{T_{im,ref,full}}{a_T} \\
\Omega_{sh,ref} = \Omega_{sh,full} a_\Omega
\end{cases}
\qquad [(3)\text{-}34]
$$

In this work, the adaptation coefficient values are set to $a_T = 1$ and $a_\Omega = \frac{1}{3}$. Therefore, the power of the physical equipment is reduced by a factor of $\frac{a_T}{a_\Omega} = 3$

3.3 Experimental validation of emulation platform

The theoretical implementation of the emulation platform was described in figure 3.8. The next step is to implement the platform in practice and to verify that its performance is acceptable. Employing the on-road efficiency map method on the emulation platform has no meaning if the platform's performance cannot be considered to correspond well to an actual EV following a drive cycle. Therefore, the verification of the platform's emulation capability is integral. The physical setup implementing the emulation platform is described in appendix C, here focus is given to the results.

The emulation capability can be considered to consist of two main requirements. First, the EIS should actuate the shaft rotation speed without significant control error. This signifies that the predetermined speed cycle of the vehicle is followed. Second, the IM should also follow its torque instruction without too much control error. The implication is that the IM generates the tractive torque that would be needed to overcome the environmental conditions and follow the drive cycle.

Figure 3.9 shows these two controlled quantities for an emulated drive cycle. No dynamometer was installed to measure the induction machine torque so an estimation using the measured stator currents and equation [(3)-16] was used to obtain it. This introduces a potential source of error that depends on the correctness of the IM parameters.
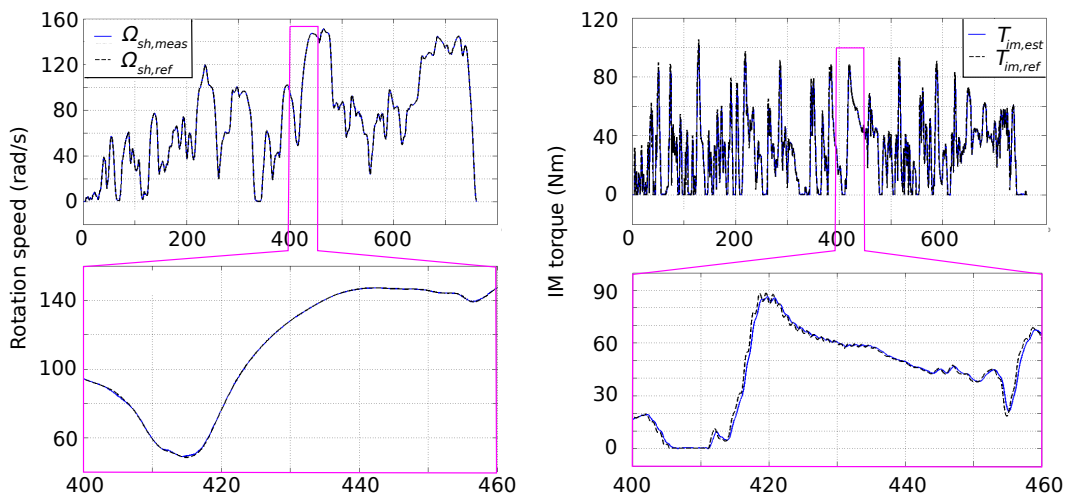

Figure 3.9: Experimental results of emulation quality.

In figure 3.9, the entire drive cycle is shown in the upper part of the figure. In the lower part, a zoom to a shorter time period is given to provide the reader a better view of the control quality. It can be seen that both the shaft speed and the induction machine torque follow their control references in a satisfactory manner. In order to follow the drive cycle and thus the shaft speed instruction without delay, the closed-loop controller controlling the vehicle speed v_{veh} has been tuned to respond quickly to the changes of the drive cycle. As can be seen from the figure, this has the effect of generating a rather aggressive IM torque instruction that at times exhibits a small ripple. Following these small variations exactly was not deemed contributing to the emulation quality. Therefore, the IM current control was tuned so that the IM drive provides a good torque response but without unnecessarily following ripple components in the torque instruction. Based on these results, the emulation platform is deemed to provide good quality of emulation. Consequently, the emulation platform can now be used as a tool to validate the on-road efficiency map method.

3.4 Conclusion

Subsections 3.1 and 3.2 of this chapter have described the general implementation of the emulation platform. Section 3.3 has verified that the practical implementation of the emulation platform is indeed capable of performing emulation of an electric vehicle with satisfactory quality. The required validation tool has therefore now been formed and its performance verified. Chapter 4 focuses on the actual validation of the on-road efficiency map method by utilizing the emulation platform.

4 Validation of on-road efficiency map method

Chapter 3 has described the emulation platform and verified the correct performance of its practical implementation. Therefore, the platform can now be used as a tool to validate the on-road efficiency map method. This validation consists of three stages, corresponding to the subsections of this chapter. First, subsection 4.1 is devoted to employing the on-road method on the emulation platform in order to deduce an efficiency map. Second, in section 4.2 the platform is modified for the classic efficiency map protocol so that a reference efficiency map can be obtained. Consequently, the validation of the on-road method can be done by a comparison of these two efficiency maps, as is the focus of section 4.3.

4.1 Efficiency map by on-road efficiency map method

The validation process is begun by obtaining an efficiency map with the on-road method. This is comparable to using the on-road efficiency map method on the real Tazzari Zero [3]. However, there will be a certain difference between the nature of the efficiency map of figure 2.4 obtained for the real Tazzari Zero, and the one that is obtained with the emulation platform. As explained, for the real Tazzari Zero, the efficiency map includes not only the effect of the electric drive but also the mechanical components. Thus, the map is plotted in the $F_{tract} - v_{veh}$ plane rather than the $T_{im} - \Omega_{sh}$ plane. However, from figure 3.8 it can be seen that this is not applicable on the emulation platform. The platform's input electrical power is a physical, reduced-power quantity while the output linear movement power is a numeric, full-power quantity. Therefore, these two powers are not comparable on the platform. To overcome this issue, the efficiency map that will be obtained with the emulation platform will exclude the mechanical parts. In any case, adding the effect of the simulated mechanical parts would not provide any more insight to the validation process. This is because the mechanical parts are not physical but modeled with the simple equations given in subsection 3.1. The efficiencies of the mechanical parts are assumed to be constant at all operating points. Thus, even if there was no power-level difference prohibiting the inclusion of the mechanical parts in the efficiency map, the inclusion of the simulated mechanical parts would simply result in the map being scaled with a constant.

Furthermore, another technical consideration affects the resulting efficiency maps. This is that the inverter's DC side current i_{inv} is not directly measured. Instead, it is estimated from the measured AC side currents by utilizing equation [(3)-1]. This is because in the measurement setup a measurement channel was not directly available

for the DC side current measurement. Equation [(3)-1] is used for the estimation with the assumption of no losses in the inverter. This results in the inverter's effect being eliminated from the efficiency map. Therefore, the efficiency map on the emulation platform is obtained for the system inside the purple box of figure 4.1. It is suggested that for future works the measurement scheme could be modified to incorporate a direct measurement of the DC current to include the effect of the inverter.
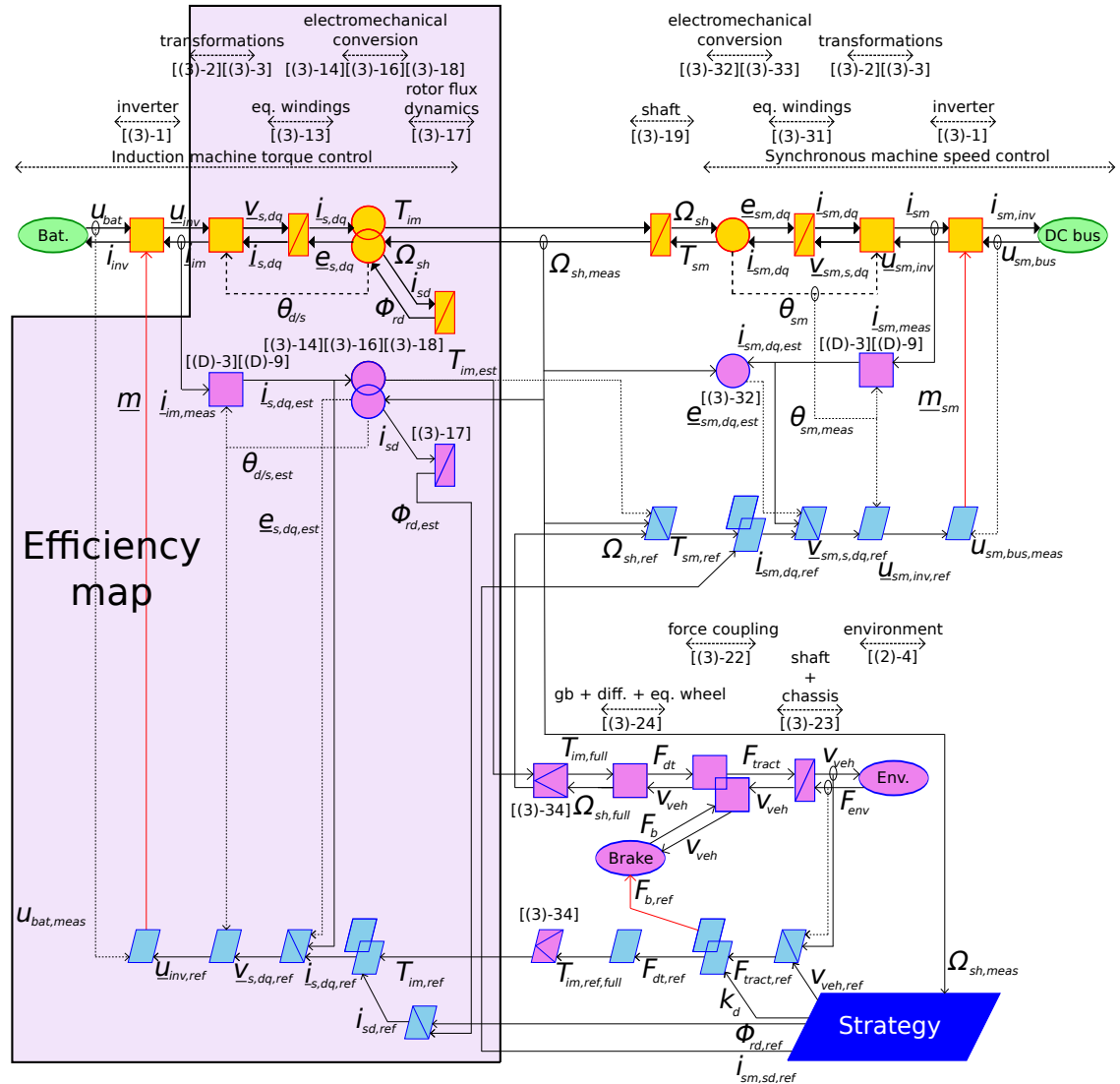

Figure 4.1: System for which the efficiency map is deduced.

The efficiency map is obtained from the drive cycle shown in figure 4.2. This is the same cycle for which the emulation quality was verified in figure 3.9. It is an extra-urban cycle that was measured using the actual instrumented Tazzari Zero. It can be seen that all major operating regions are covered, including strong accelerations

and a high-speed part where the vehicle sustains its near-maximum speed for some time. Consequently, a priori it should be a well suited driving cycle for the on-road efficiency map method.
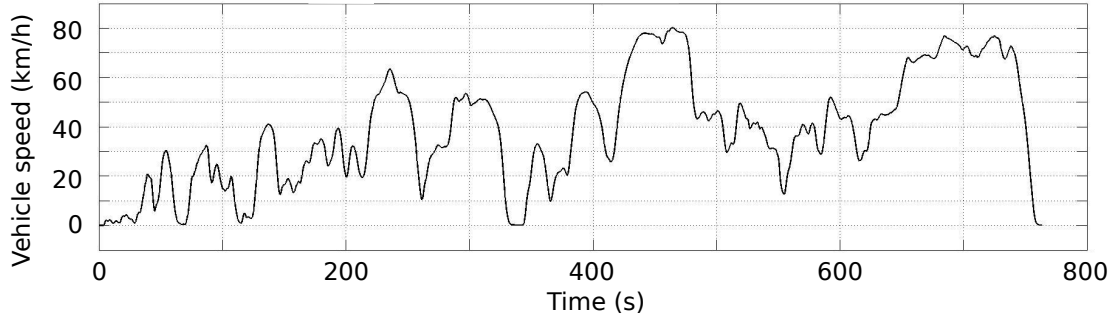
Figure 4.2: Vehicle speed cycle used in efficiency map deduction.

Figure 4.3 shows the main quantities of interest during the cycle. On the left, the input electrical power quantities are shown in blue. In the emulation platform, the drivetrain's battery is implemented by a DC bus. Some voltage variations during the cycle are visible. This is due to the IM drive taking electrical power stored in the DC bus capacitor faster than it is recharged from the mains. The electrical input power is formed as the product of the DC bus voltage u_{bat} and the current i_{inv} drawn from the bus (estimated from the inverter's AC side currents as explained above). It is seen that the IM drive draws current even when zero torque is produced. This is because the induction machine is magnetized by the stator currents even when no torque is required. The right side shows the mechanical output power quantities - the shaft rotation speed and the IM torque. The formed input electrical and output mechanical powers are plotted together in the second plot from the bottom. It shows how the electrical and mechanical powers mostly have the same shape with the difference of the curves representing the power losses. Finally, the efficiency of the energy conversion during the cycle is shown in the bottom plot.

An efficiency map can be deduced based on the results of figure 4.3. Measurements are taken at various torque-speed operating points and an efficiency is computed for each point according to [(2)-1]. A continuous efficiency map is then obtained by means of interpolation and extrapolation. The result is shown in figure 4.4. The black dots represent measured operating points while the rest of the values are results of interpolation and extrapolation.
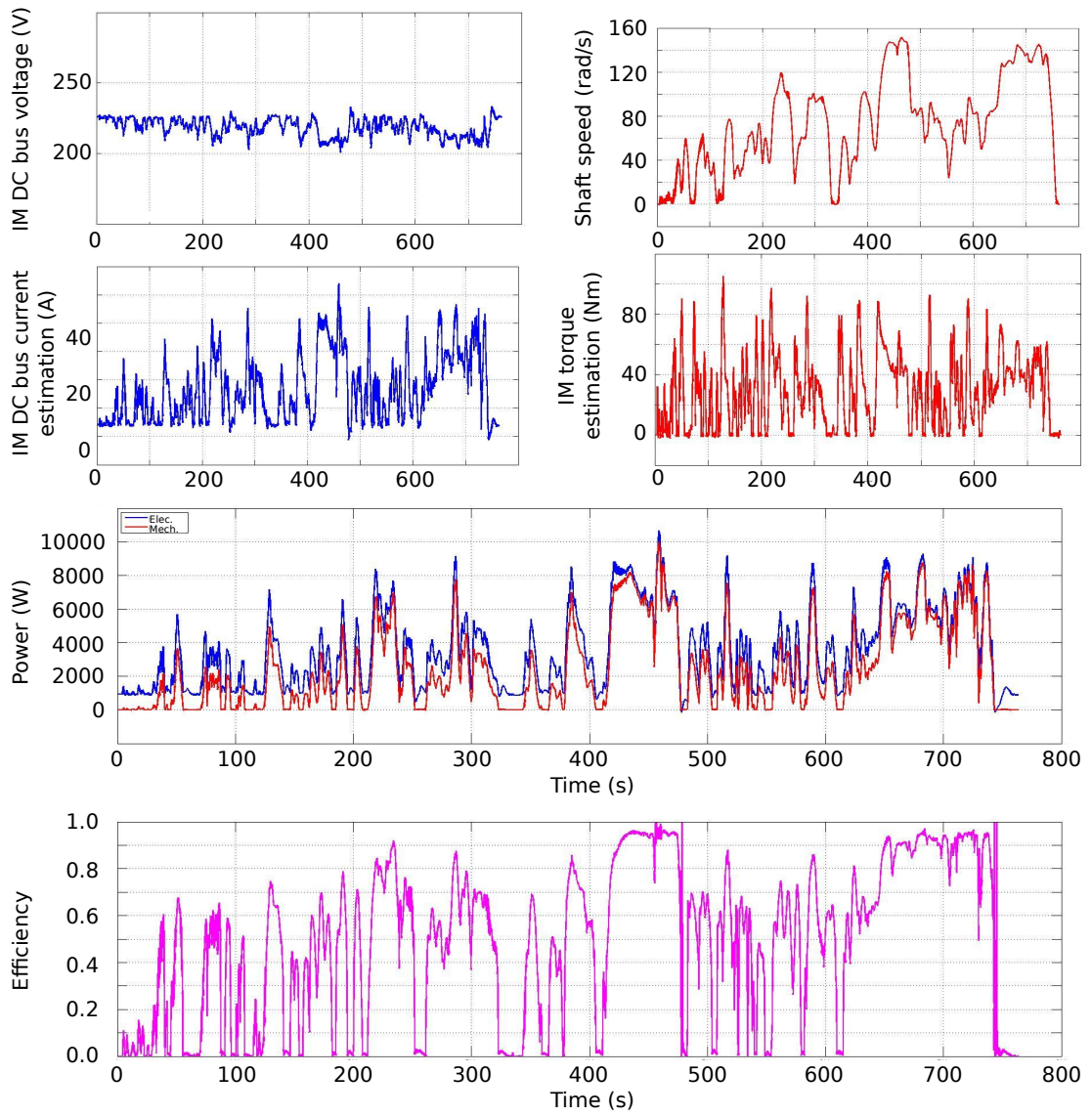
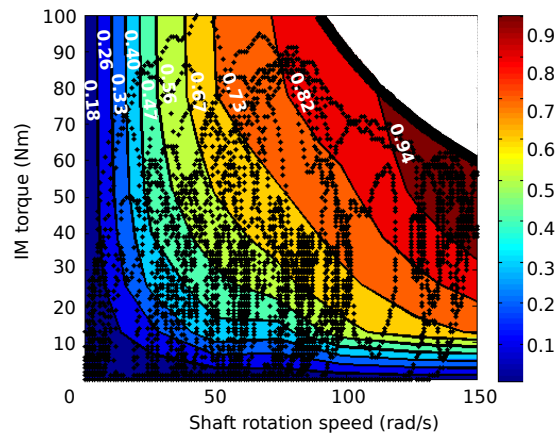Figure 4.3: Computing the efficiency from input and output powers.

Figure 4.4: Efficiency map obtained with the on-road method from an emulated drive cycle.

The highest efficiencies are observed at flux weakening speeds with relatively high torques. This is logical since the relative significance of the magnetization current decreases compared to the torque producing current. The low efficiencies at low torques and speeds can be explained by recalling that the IM still needs to be magnetized even when the mechanical power is low, i.e. at low torques and speeds. The flux weakening strategy described in appendix F controls the machine flux to the nominal value when the machine is not operated in field weakening. Thus, the flux producing current is relatively more significant at low mechanical power. In other words, electrical power is still needed for the magnetization even when produced mechanical power is low.

Finally, one important remark is made about this efficiency map. Notable differences can be found when comparing the efficiency map of figure 4.4 to the efficiency map of the actual Tazzari Zero in figure 2.4. First, it should be emphasized that the efficiency map of the real Tazzari Zero includes the effect of the mechanical parts and the inverter while the emulation platform excludes them. This could change the distribution of the efficiencies as in reality the mechanical parts and the inverter exhibit operating point-dependant efficiency variation. Second, while the emulation platform employes an electrical drive that is fundamentally of the same type as in the Tazzari Zero; the actual machine and inverter specifications are quite different[20]. The emulation platform IM drive consists of an industrial IM fed by a general-purpose VSI. In contrast, the Tazzari Zero's electrical drive has been specifically designed for the vehicle. As the physical equipment used in the Tazzari Zero and the emulation platform are not the same, the resulting efficiency maps cannot be expected to be identical. Third, the flux weakening strategy of the real Tazzari Zero is unknown. Also this has an effect on the efficiency map since magnetization of the machine requires electrical power.

However, these differences do not prohibit the validation of the on-road method. The validation is based on being able to employ the on-road method and the classic protocol on a system that can be considered equivalent to the actual Tazzari Zero. This is the case, as the platform has the same fundamental structure as the Tazzari Zero. An exact match between the efficiency maps of the emulation platform and the Tazzari Zero is not necessary for the validation of the on-road method.

---

[20]The specifications of the Tazzari Zero are presented in appendix A while the emulation platform specifications can be seen in appendix C.

4.2   Efficiency map by classic protocol

The next step towards validation of the on-road method is to obtain a reference efficiency map. This is done by utilizing the classic efficiency map protocol illustrated in figure 2.3. This requires modifications to be made to the platform shown in figure 3.8. In emulation usage the PMSM drive's shaft speed instruction $\Omega_{sh,ref}$ and the IM drive's torque instruction $T_{im,ref}$ are generated by the simulated part of the drivetrain and its control. They result from the predetermined drive cycle and imposed environmental conditions as well as the tuning of the drivetrain control. However, to employ the classic protocol on the platform, these control references instead need to be directly determined. Therefore, for the classic protocol the emulation platform is modified to the version shown in figure 4.5. The efficiency map is of course obtained for the same system as with the on-road method, illustrated in figure 4.1.

In order to cover enough operating points, the IM torque and PMSM shaft speed references were chosen as shown in figure 4.6. A speed range of 0-157 rad/s was used, divided into 14 different speed operating points for a resolution of about 12 rad/s between consecutive speed values. A torque range of 0-100 Nm was used, also with 14 different torque operating points used for a resolution of approximately 7.7 Nm between consecutive torque values. These ranges were selected to cover all the operating regions that were present in the efficiency map obtained with the on-road method in figure 4.4. The choice of using 14 operating points for both the speed and torque was deemed to give enough operating points to construct an efficiency map of high quality without relying too much on interpolation. The figure shows that the control quality of both speed and torque is good. A small oscillation of shaft speed can be seen with a few torque-speed combinations but this is considered minor.
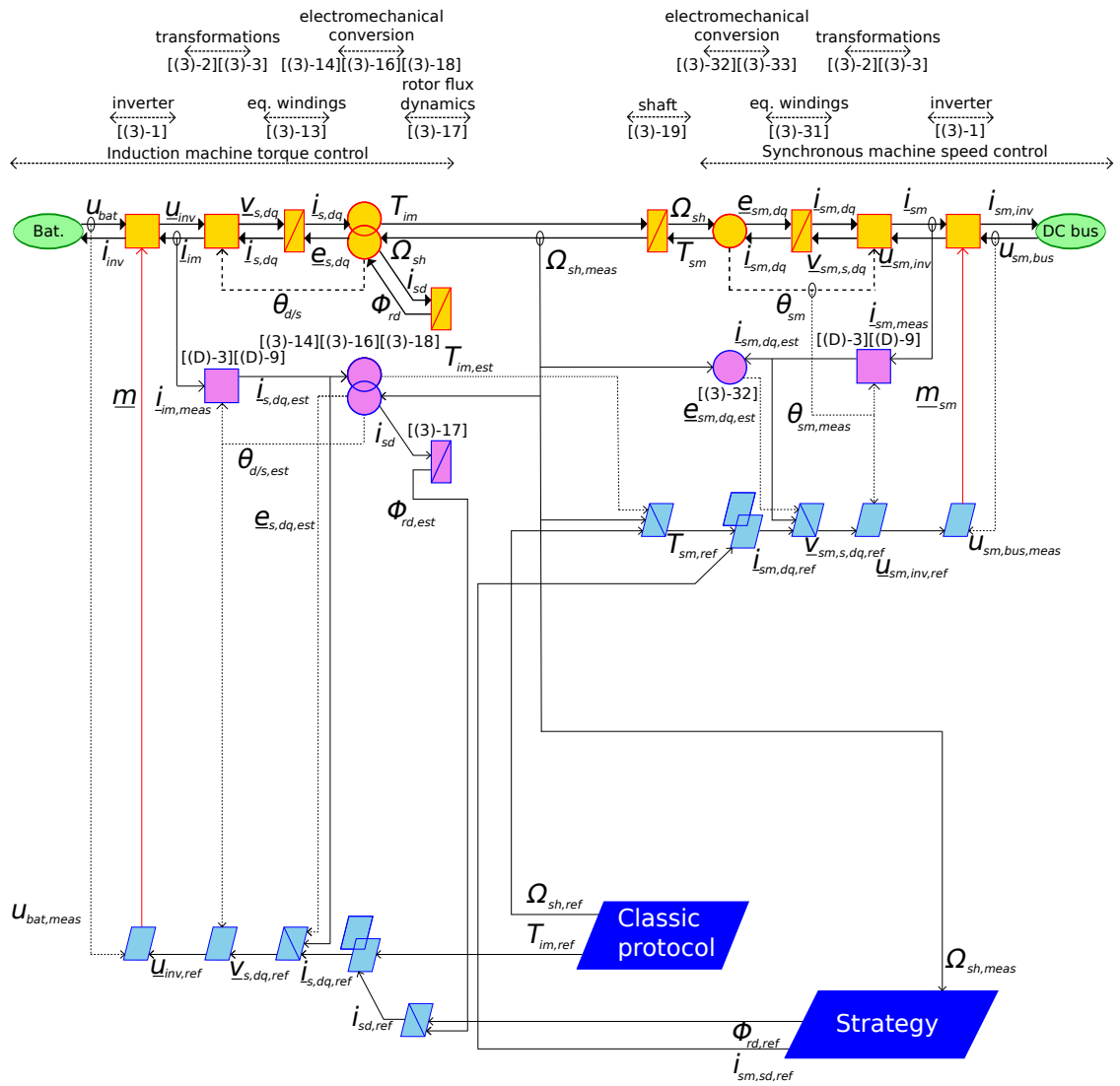
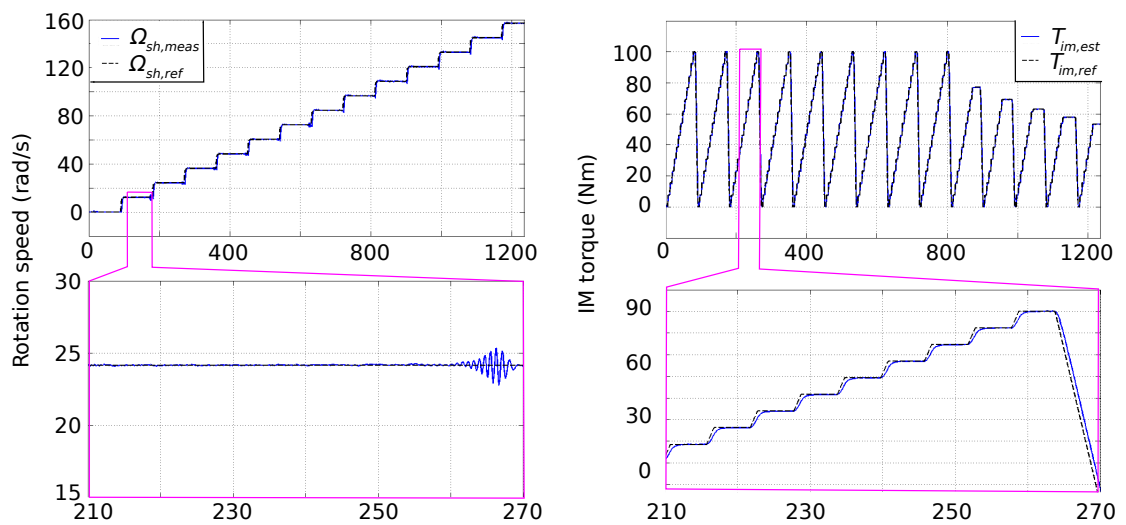Figure 4.5: Emulation platform modified for the classic protocol.

Figure 4.6: Classis protocol measurement cycle.

The cycle shown in figure 4.6 enables measuring a sufficient number of operating points to construct an efficiency map. In contrast to the on-road efficiency map method, measurements are only taken in steady state operation, i.e. when the speed and torque of the machine are no longer changing significantly. This is illustrated below in figure 4.7 where each taken measurement point is indicated with a red line (all of the protocol cycle is not shown). Each of these measured operating points can then be used in the construction of an efficiency map by the classic protocol. In flux weakening operation, the maximum required torque references are decreased to avoid overloading the drive.
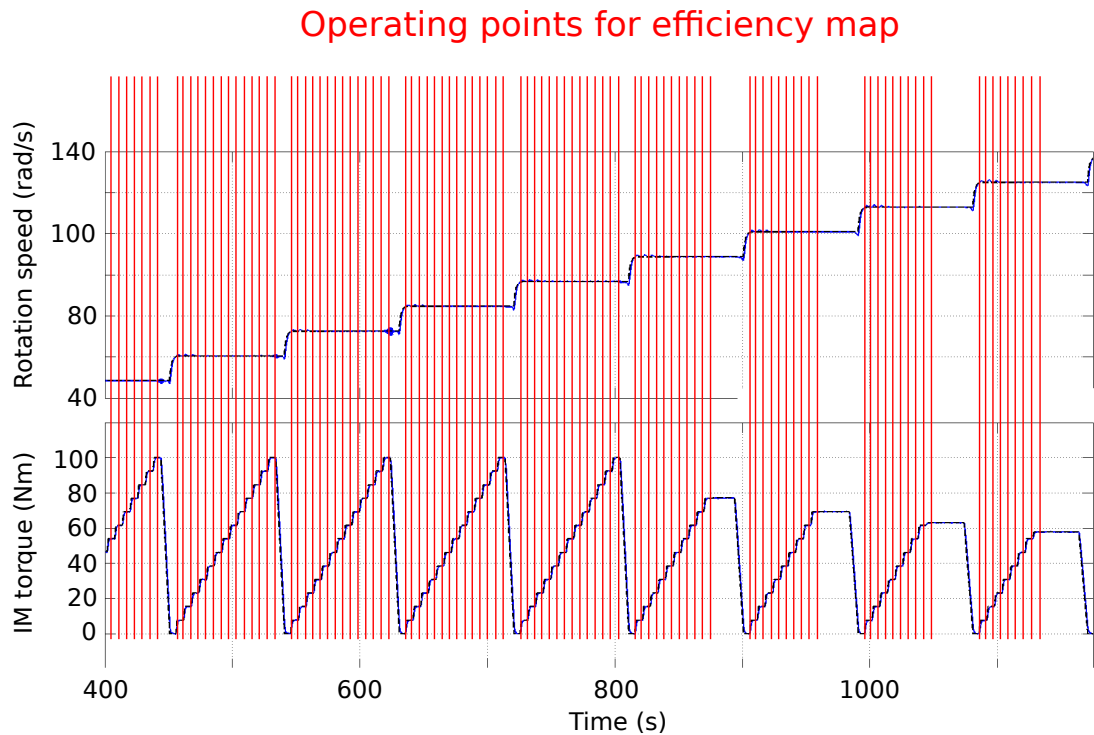
Figure 4.7: Illustration of how operating point measurements are taken for constructing the classic protocol efficiency map. An operating point measurement is taken at the points indicated by a vertical red line.

The efficiencies of the measured operating points are computed exactly as in the on-road method in section 4.1. The continuous efficiency map shown in figure 4.8 is obtained by interpolation between the measured operating points.

The efficiency map clearly shows how the operating points (black dots) are distributed homogenously and systematically across the efficiency map. This is in contrast to the operating point distribution of the on-road efficiency map method where the operating point locations are determined by the drive cycle and environmental conditions.
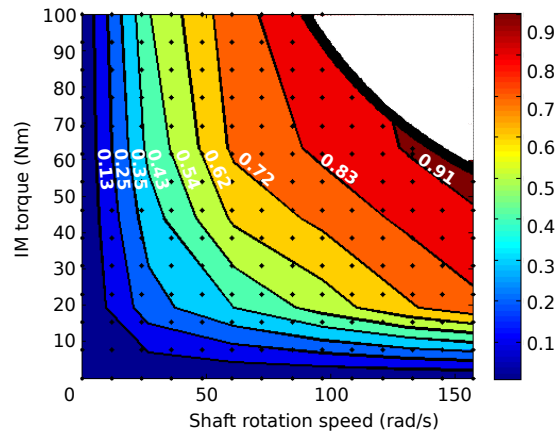
Figure 4.8: Efficiency map obtained with the classic protocol.

4.3 Comparison of efficiency maps

Having obtained an efficiency map by the on-road method and with the classic proto-
col, it is now possible to evaluate the differences between the two efficiency maps.
Once again, it is recalled that the most fundamental difference between the two
methods is how operating point measurements are obtained. In the efficiency map
obtained from the classic protocol, operating points are taken only from steady state.
This reflects the nature of an efficiency map in general as it is a static model of a
system. Thus, its purpose is to describe a system operating in steady state with no
consideration for transient states. In contrast, the on-road efficiency map method
also produces an efficiency map but from measurements made during a dynamic
drive cycle where operation is mostly in transient states. In other words, the on-
road method produces a static description of a system based on measurements made
in dynamic operating conditions. The goal of this Master's Thesis and this section is
to investigate whether the dynamic operating conditions used in the on-road method
significantly distort the resulting efficiency map.

Figure 4.9 shows the absolute error between the efficiency maps of figures 4.4 and
4.8. It can be seen that in general the error remains mostly under 8%, in many
places below 4%. The largest errors are found at flux weakening speeds with rela-
tively low torque. The maximum obtained error reaches approximately 14% although
this error magnitude region is small. A likely reason for the region with more error
is that in the emulated cycle only a limited number of operating points were recorded
in this part of the efficiency map. This is seen from figure 4.4 as a small number of
black dots. This highlights the importance of having an appropriate drive cycle for
using the on-road efficiency map method. For example, if the drive cycle does not

contain high speeds or only soft accelerations are made, operating points will not be obtained for some parts of the efficiency map. This is especially problematic if operating regions at the edges of the efficiency map are not covered by the drive cycle. For such regions, the on-road method must rely on extrapolation which has always more uncertainty than interpolation. Therefore, extrapolated areas of operation that are far from actual measured operating points have more risk of error than interpolated operating regions. Consequently, significant use of extrapolation is expected to increase the error in the resulting efficiency map. The drive cycle shown in figure 4.2 has provided operating points in most, but not all parts of the efficiency map. Thus, it is rather well suited for the on-road method although not completely ideal.
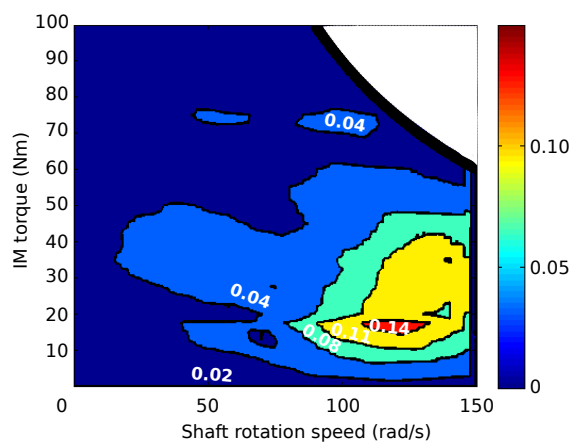

Figure 4.9: Difference between the efficiency maps of figures 4.4 and 4.8.

To further examine whether the error shown in figure 4.9 is significant or not, the performance of the two efficiency maps are compared on another drive cycle on the emulation platform. It is recalled from chapter 2 that the larger research project is focused on energetic studies of the vehicle. The advantage of the on-road method would be to provide a static model for the Tazzari Zero that could be used in such studies. Therefore, the energetic performance of the two efficiency maps is next examined. Another drive cycle is used for this, shown below in figure 4.10.

The energetic comparison is done as follows. The actual energy consumption serves as the reference point for the energy consumption predictions of the two efficiency maps. This actual consumption is shown in blue on the top plot of figure 4.11. It is obtained as the time integral of the consumed electric power. This power is measured on the platform as the product of the DC bus voltage and current feeding the induction machine. The energy consumption predicted by the on-road method efficiency map and the classic protocol efficiency map are shown with the dashed red line and
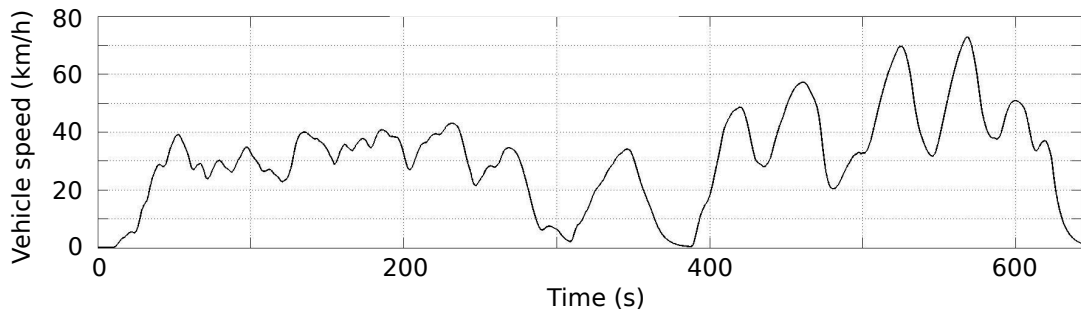
Figure 4.10: Drive cycle used for the comparison of the energetic performances of the two efficiency maps.

the dotted green line, respectively. Knowing the mechanical operating point throughout the cycle, the respective efficiency maps give the electrical power needed for the electromechanical energy conversion at each point of the cycle. The respective energy consumptions are then obtained as the time integrals of the predicted electrical power consumption profiles. The bottom plot of figure 4.11 shows the evolution of the relative error of the two efficiency maps compared to the actual consumption.

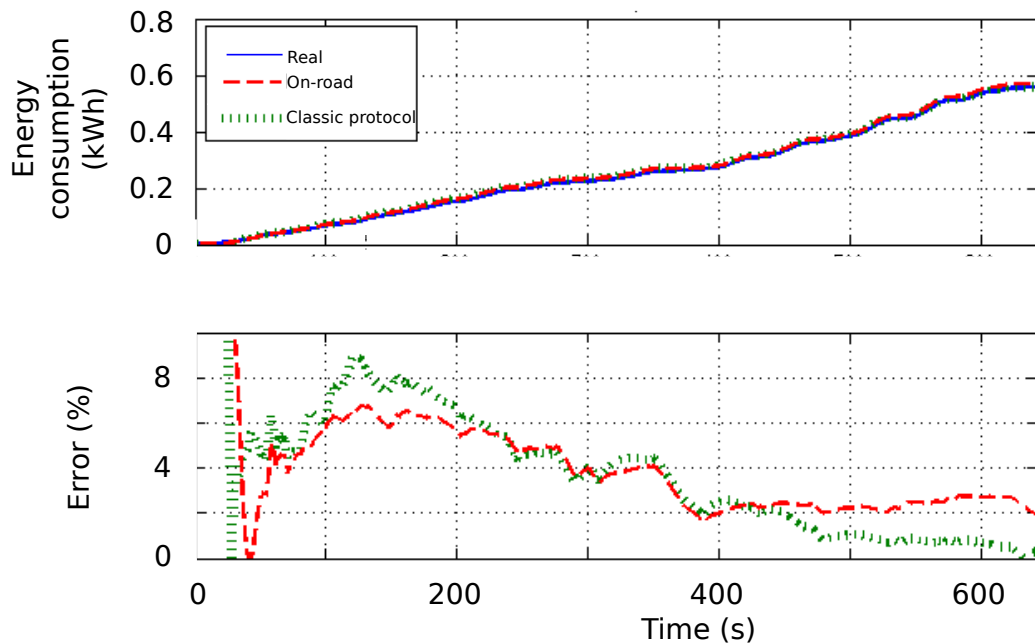The figure shows that at the end of the cycle, the total energy consumption predicted

Figure 4.11: Energy consumption comparison between the actual consumption, the prediction by the on-road method efficiency map and the prediction by the classic protocol efficiency map.

by both efficiency maps is very close to the actual consumption. The classic protocol efficiency map finishes with a predicted energy consumption of 0.3% lower than the actual consumption. The efficiency map obtained with the on-road method results in a total energy consumption prediction that is 2% higher than the actual consumption. In the beginning of the cycle, the relative error of the efficiency maps is significant but as the cycle progresses, the overall error clearly has a tendancy to cancel out. Based on these results, the static model of an efficiency map seems to be capable of describing the energetic behaviour of a traction electric drive with good accuracy on a global level. Errors made by the efficiency maps tend to cancel out during long drive cycles. This good global performance is indeed the idea in the research project. Additional advantages of efficiency maps are that they are computationally very light[21] but still describe the main aspect of the energy conversion, i.e. the efficiency. Consequently, an efficiency map can be used for example for simulations of the vehicle performance in different drive cycles and environmental conditions or for testing different energy management strategies. However, overly detailed conclusions should not be made for very short time periods as instantaneous errors may be much more significant. Moreover, fundamentally an efficiency map offers no insight to what occurs in transient states or where control problems may appear. Understanding the advantages and limitations of efficiency maps is crucial for using them in appropriate situations.

From an energetic perspective, the energy consumption predicted by the two efficiency maps behaves very similarly. Therefore, the dynamic operating conditions used in obtaining the efficiency map in the on-road method are seen to have only a minor effect on the global energy consumption prediction. In view of the goal of describing the global energetic performance of a traction electrical drive, it is therefore confirmed that the on-road efficiency map method's dynamic measurement conditions do not result in a significant error.

4.4 Conclusion

The goal of this chapter has been to present the experimental results that partially validate the on-road efficiency map method. This was enabled by the emulation platform whose implementation was described in chapter 3. The actual validation consisted of three stages. First, in section 4.1 the on-road efficiency map method was employed on the emulation platform in order to obtain an efficiency map. This was comparable to using the on-road method on the real Tazzari Zero. Second, in section 4.2 a reference efficiency map was obtained by using the classic efficiency map

---

[21]Computationally, an efficiency map is basically a simple look-up table of efficiency values for different operating points.

protocol described in figures 2.3 and 4.5. Both of these methods construct the efficiency map based on measured operating points for which efficiencies are computed. The fundamental difference between the two methods is how measurements of the operating points are made. In the classic efficiency map protocol, measurements are taken only in steady state operation. In contrast, the on-road method makes use of measurements taken during dynamic operation of the drive cycle. The goal of this Master's Thesis has been to investigate whether these dynamic measurement conditions have a significant distorting effect on the resulting efficiency map.

Section 4.3 presented the comparison of the two efficiency maps. It was shown that while some differences were found between the two efficiency maps, these differences were mostly minor. In figure 4.11, the two efficiency maps were then used on another drive cycle to predict the energy consumption of the system. It was shown that while conclusions based on individual operating points and short time periods should be avoided, the global energy consumption predictions of both the efficiency maps were very close to the actual consumption. Therefore, the dynamic measurement conditions of the on-road method do not result in a significant error in the resulting efficiency map.

5 Conclusion and perspectives

This Master's Thesis aimed at the experimental validation of the on-road method. To achieve this, an emulation platform was implemented as a validation tool. The platform was based on Hardware-In-the-Loop simulation of an electric vehicle where the electrical drive of the drivetrain was implemented with physical equipment and the mechanical parts by real-time simulated mathematical models. An emulation interface system, consisting of another electrical drive, needed to be implemented in order to connect the physical and simulated parts of the setup. Energetic Macroscopic Representation was used as a design tool in order to organize the complexity of the mathematical model and to provide a systematic procedure for control design. The implemented emulation platform allowed employing both the on-road method and the classic efficiency map protocol to obtain two efficiency maps. The main difference between these two methods was that in the on-road efficiency map method, operating point measurements were obtained from the dynamic operating conditions of a drive cycle while in the classic protocol measurements were only taken from steady state operation.

Obtaining these two efficiency maps by using the emulation platform showed an error of mostly under 8%. A larger error of 10-15% was obtained for high speed operation with relatively low torque. However, this may have been due to the small number of operating points recorded in this region when using the on-road method. This highlighted the importance of a varied drive cycle when using the on-road efficiency map method. If the drive cycle does not result in operating points recorded in all parts of the efficiency map, the on-road method must rely heavily on interpolation and extrapolation. This increases the risk of significant errors in the resulting efficiency map. Finally, an energetic comparison was performed on the platform in order to evaluate the accuracies of the two efficiency maps. Here, the two maps were used to predict the energy consumption of an electric vehicle during a drive cycle. Both efficiency maps yielded an energy consumption prediction within 2% of the actual consumption. Thus, the efficiency map of the on-road method seems to give practically the same global results as the efficiency map obtained from the classic protocol. In addition, the results confirmed that for energetic purposes, an efficiency map gives accurate results on a global level. On the other hand, overly detailed conclusions for short periods of operation should be avoided as efficiency maps may result in more significant instantaneous errors.

While the dynamic operating conditions of the on-road efficiency map method have not been found to result in large errors in the efficiency map, other aspects of the

method still remain to be investigated before it can be considered entirely validated. Most importantly, the effect of the tractive force estimation should be examined. This estimation depends on several parameters of the vehicle and of the environment. There is most likely some error associated with the parameter values that are used for the real Tazzari Zero. Thus, it should be determined how sensitive the on-road efficiency map method is to errors in the environmental and vehicle parameters. In addition, the tractive force estimation includes computing a numeric derivative of the measured vehicle speed. This could also have a detrimental effect on the estimation quality.

Some limitations exist related to the performed validation. First, in the emulation platform, the mechanical parts of the vehicle drivetrain were implemented by real-time simulated mathematical models rather than physical components. These models cannot be expected to describe the mechanical behaviour with perfect correspondance to physical components. Second, the IM torque that was necessary for deducing efficiency maps was estimated rather than measured. This estimation is sensitive to the correct knowledge of the IM parameters. Although using this same means of estimation for both efficiency map methods made the results comparable, more reliable efficiency map results would necessitate the use of a dynamometer to measure the IM torque. Third, the IM inverter DC side current was estimated from the measured AC side currents rather than being directly measured. This estimation assumed ideal operation of the inverter and thus removed its effect from the efficiency maps. Modifying the measurement setup to enable direct measurement of the DC side current would enable including the effect of the inverter in the efficiency maps.

The complete validation of the on-road method would enable obtaining a valid model for the real Tazzari Zero. This would provide a valuable tool for investigating possible improvements to the vehicle. For example, it could be investigated how adding hybrid energy storage in the form of supercapacitors or fuel cells would affect the vehicle's energy economy or battery lifetime [40, 41]. As for the on-road method itself, it could be extended to include the regenerative braking strategy of the Tazzari Zero.

A   Tazzari Zero characteristics

The Tazzari Zero [23] is a commercially available small battery electric vehicle. It is powered by a 80 V - 160 Ah Lithium Iron Phosphate (LiFePO4) battery pack that consists of 24 individual cells connected in series. This same battery pack also powers the vehicle's auxiliaries through a DC/DC converter. The traction electrical machine of the Tazzari Zero is a 15 kW induction machine that the battery pack supplies through a VSI. The machine shaft's rotation speed is reduced by a single-ratio gearbox. It is connected to the rear-axle of the vehicle via the mechanical differential. The rear-axle's two driven wheels then convert the rotational movement of the axle to linear movement of the vehicle. Mechanical brakes are included for safety and because the regenerative braking capacity of the vehicle is limited. The drivetrain of the vehicle is shown in figure 2.2.

The vehicle has been instrumented with a data acquisition system. Electrical sensors measure the current and voltage of the battery pack while a GPS antenna provides data of the vehicle velocity and changes in altitude. The battery current and voltage measurements include filtering. The central unit of the acquisition system (Compact RIO, National Instrument) has been installed in the trunk of the vehicle and obtains synchronized measurement data at intervals of 0.5 s. Table A.1 shows the values of Tazzari Zero parameters used in the work. In addition, the values of environmental parameters relevant to equation [(2)-4] are shown.
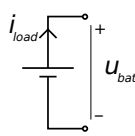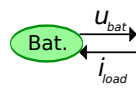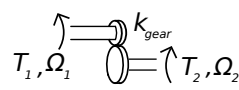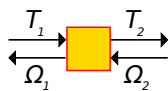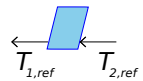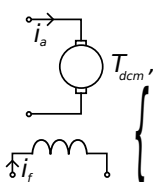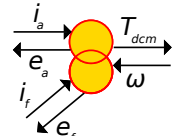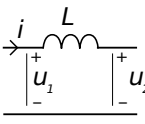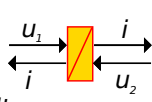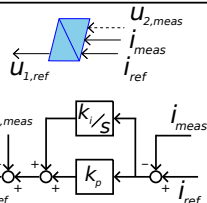
Table A.1: Tazzari Zero and environmental parameters used in the work.

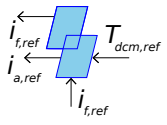| Parameter name	Symbol	Value
Total speed reduction of transmission	$k_{diff}k_{gear}$	5.84
Total efficiency of transmission	$\eta_{diff}\eta_{gear}$	96%
Wheel radius	r_{wh}	0.2865 m
Kerb mass	m_{kerb}	562 kg
Driver mass	m_{driver}	60 kg
Total equivalent mass with driver	M_{tot}	622 kg
Equivalent friction coefficient of shaft	B_{tot}	38.27 Ns/m
Rolling resistance coefficient	c_{roll}	0.02
Standard gravitational acceleration	g	9.81m/s^2
Air density at 20 C°	ρ	1.223 kg/m^3
Aerodynamic coefficient	$c_{drag}A$	0.7 m^2
Wind velocity against vehicle movement	v_{wind}	0 m/s
Slope angle	α	0°

B EMR basic examples

Section 2.4 has outlined how EMR can be used to organize the mathematical representation of a complex system and to systematically obtain a control structure for the system. The goal of this appendix is to supplement section 2.4 by providing simple examples of each type of EMR element in table B.1. In addition, a corresponding control element for each of these EMR elements is shown in the table.

Table B.1: Examples of EMR elements and their corresponding control elements.

EMR element	Example	Control element
Source element	Ideal battery	
Conversion element	Ideal mechanical gear $\begin{cases} T_2 = k_{gear} T_1 \\ \Omega_1 = k_{gear} \Omega_2 \end{cases}$	$T_{1,ref} = \dfrac{T_{2,ref}}{k_{gear}}$
Coupling element	Externally excited DC machine $\begin{cases} T_{dcm} = k_{dcm}\, i_f\, i_a \\ e_a = k_{dcm}\, i_f\, \omega \\ e_f = 0 \end{cases}$	$i_{a,ref} = \dfrac{T_{dcm,ref}}{k_{dcm}\, i_{f,ref}}$
Accumulation element	Ideal inductor $\quad u_1 - u_2 = L\dfrac{di}{dt}$ $\Downarrow$ $i = \dfrac{1}{L}\int (u_1 - u_2)\,dt$	

First, an example of a source element is given as an ideal battery that provides a constant voltage u_{bat} to the connected system. This is the action variable of the element since the battery is a voltage source. The reaction variable is the current i_{load} that is drawn by the connected load.

Second, an ideal mechanical gear is taken as an example of a conversion element. The gear linearly modifies the torque and rotation speed between the two connected shafts. The equations describing this component are shown in the table and are the

contents of the shown EMR conversion element[22]. The control element of an EMR conversion element can be obtained by a direct inversion, i.e. a reformulation of the model equation. This is shown in the table by the light blue control element, in this case assuming that the quantity to control is the EMR element's output torque T_2.

Third, a coupling element is exemplified in the table by the electromechanical conversion of an externally excited DC machine[23]. The torque of the machine is the mechanical output. It is seen to depend not only on the armature current i_a but also on the field winding current i_f that is proportional to the flux of the machine. Moreover, the machine develops a back emf e_a in the armature circuit as a response to the shaft rotation angular frequency ω. The back emf is the reaction variable of the element on the electrical side. There is no back emf generated to the field winding circuit so $e_f = 0$ (but EMR conventions require elements to be connected by an action-reaction variable pair so it is displayed). There is a degree of liberty in the control of the electromechanical conversion since the same torque can be produced with different value pairs of $\{i_a, i_f\}$. In EMR, this degree of liberty becomes apparent as one of the two currents becomes a strategy-level input and the other is used to control the torque. In a practical DC machine application, this is done so that i_a controls the torque and i_f is determined by the flux-weakening strategy.

Fourth, an ideal inductor is used as an example of an accumulation element. Since the mathematical model of the inductor is a differential equation, it is represented by an accumulation element. The form required by EMR is obtained by formulating the equation so that the outputs of the element are integral functions of the inputs. Note that both the outputs of the element are the same current i. Unlike other EMR elements, the corresponding control element of an accumulation element cannot be obtained by a reformulation of the model equation. That would require a control element whose output is a derivative function of the input, and this is not allowed in EMR. Therefore, an indirect inversion is used by employing a closed-loop controller. One example of this is a PI controller with disturbance compensation[24] of u_2 as shown in the table. The indirect inversion of an accumulation element always requires the measurement of the accumulation element output.

---

[22]The equations could also be organized to have $\{T_2, \Omega_1\}$ as inputs and $\{T_1, \Omega_2\}$ as outputs. Indeed, the inputs and outputs of conversion elements can be arranged in different ways without conflict with the EMR causality principle. This is in contrast to accumulation elements that have fixed inputs and outputs due to the temporal relations they represent. In fact, typically the accumulation elements of a given system determine how the inputs and outputs of other elements should be defined.

[23]Note that this does not include a description of how currents i_a and i_f have been generated. Other EMR elements would be used to describe how these currents are induced by applying voltages to the windings of the machine.

[24]This compensation is not obligatory since a closed-loop controller can simply be made to reject the disturbance.

C eV experimental platform

The emulation platform and all experimentation of this work was performed in the L2EP laboratory on the so called eV experimental platform. The eV platform consists of a variety of equipment available for experimentation, including electrical machines, VSI's, supercapacitors and fuel cells. Their modular arrangement enables them to be connected to create experimental setups as needed by different research projects. The goal of this appendix is to describe how the eV platform was used in order to implement the emulation platform of this work. In addition, the parameter values of the emulation platform's physical equipment are given.

As can be seen from figure 3.8, the physical equipment of the emulation platform consists of the IM and the PMSM as well as their electrical supplies. Figure C.1 presents the same EMR diagram but with the actual physical equipment of the implementation shown. The remaining elements of the figure represent the real-time simulation of the mechanical parts of the drivetrain as well as the control of the drivetrain and the PMSM drive. All these real-time functions are implemented by a dSpace 1005 controller board. In the experimental results of this work, a computation frequency of 10 kHz was used.

As mentioned in chapter 4, the function of the IM drive's battery is implemented by a DC bus. Both of the DC buses of the platform are separate and created in the following way. The three-phase mains voltage output is connected to an autotransformer that allows regulating the amplitude of the three-phase voltages. The three-phase voltage output of the autotransformer is then rectified by a full diode bridge and the resulting DC voltage is smoothed by the DC bus capacitors. Creating a DC bus in this way allows easy manual regulation of the DC voltage level by altering the transformer voltage ratio[25]. However, it is also the reason why the emulation platform is implemented with reduced power compared to the Tazzari Zero. The power reduction is not due to machine limitations but comes from the autotransformers. While the nominal stator currents of the two machines are 41.8 A and 43 A respectively, the maximum allowed current RMS values of the two respective autotransformers are 20 A and 22 A. Thus, reduced power is used to ensure safe operation[26].

---

[25]This capability allows limiting the inrush currents of the DC bus capacitor when connecting the mains to the rectifier feeding the DC bus capacitor.

[26]Another possibility would be to feed both the IM and the PMSM inverters from the same DC bus. This would drastically reduce the electrical power taken via the autotransformer. In the typical situation where the IM generates positive torque and the PMSM negative torque to impose resistive forces, the regenerative braking energy of the PMSM could be directly used by the IM instead of being converted to heat with a large resistor. However, using one DC bus was discovered to result in strong variations of the DC bus level which in turn was problematic for the control of the inverters. Consequently, two separate DC buses were used in this work.
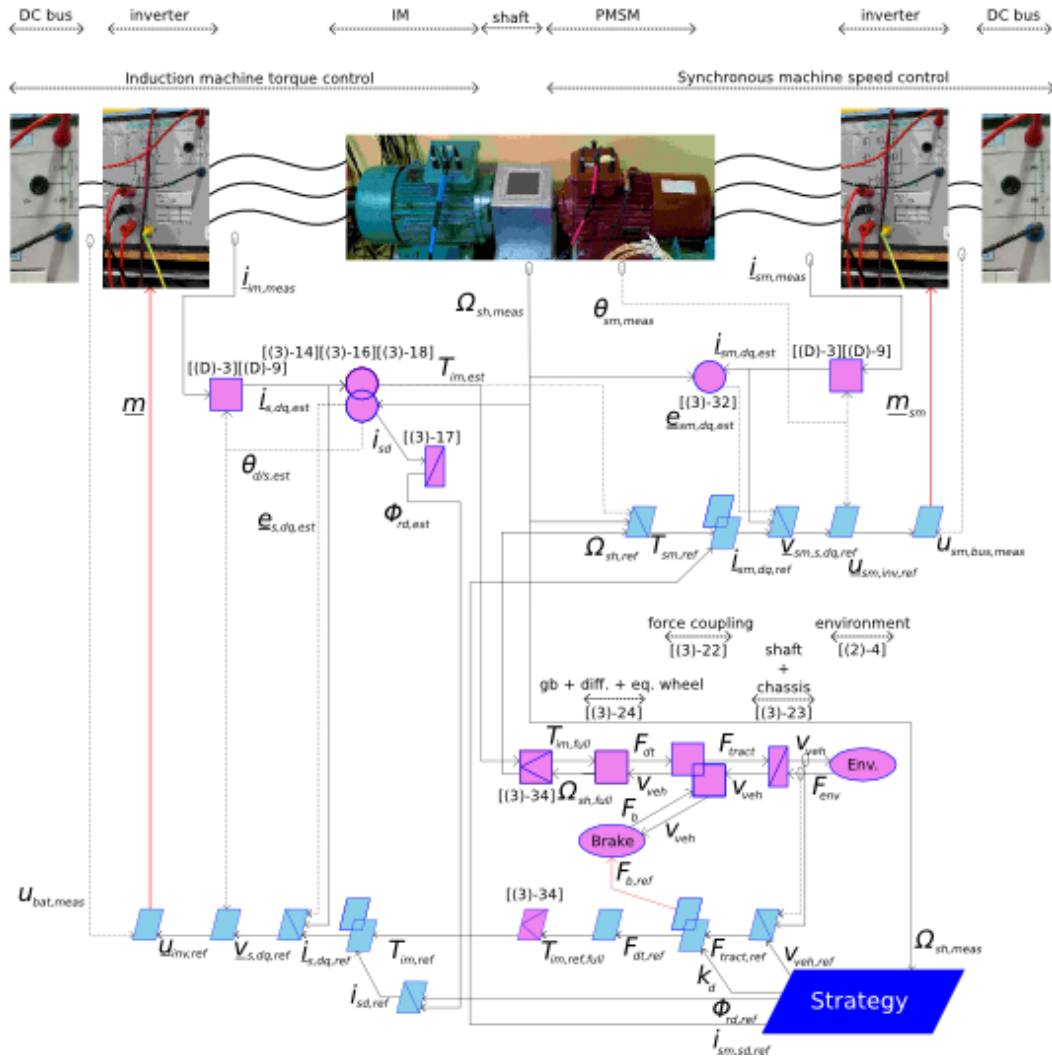
Figure C.1: Emulation platform implementation on the eV platform in the L2EP laboratory.

Physical measurements are implemented as follows. The DC bus voltages are measured by two voltage probes. Two AC line currents are measured from each inverter using measurement sensors integrated directly into the inverters, providing $\underline{i}_{im,meas}$ and $\underline{i}_{sm,meas}$. A tachometer is used to provide the speed measurement $\Omega_{sh,meas}$ as well as the shaft rotation angle that is also the measured PMSM rotor position $\theta_{sm,meas}$. All these measurements are then given to the dSpace controller board.

The platform's induction machine has a squirrel cage rotor and parameter values as shown below in table C.1.

Table C.1: Induction machine parameters.

Parameter name	Symbol	Value
Number of pole pairs	p	2
Stator resistance of one phase	R_s	0.35 Ω
Rotor resistance	R_r	0.45 Ω
Stator self inductance of one phase	L_s	0.0503 H
Rotor self inductance	L_r	0.0503 H
Mutual inductance between one stator phase and rotor	M_{sr}	0.0447 H
Nominal output power	P_{nom}	22 kW
Nominal line-to-line RMS voltage	U_{nom}	400 V
Nominal stator winding current	I_{nom}	41.8 A
Nominal stator angular frequency	$\omega_{d/s}$	$2\pi 50$ rad/s
Nominal rotation speed	N_{nom}	1456 rpm

The permanent magnet synchronous machine parameters are shown in table C.2.

Table C.2: Permanent magnet synchronous machine parameters.

Parameter name	Symbol	Value
Number of pole pairs	p	4
Stator resistance of one phase	R_s	0.41 Ω
Stator d-axis inductance	L_d	0.0081 H
Stator q-axis inductance	L_q	0.0101 H
Permanent magnet flux crossing the airgap	Φ_{pm}	1.1905 Wb
Nominal output power	P_{nom}	22.8 kW
Nominal line-to-line RMS voltage	U_{nom}	360 V
Nominal stator winding current	I_{nom}	43 A
Nominal stator angular frequency	$\omega_{d/s}$	$2\pi 100$ rad/s
Nominal rotation speed	N_{nom}	1500 rpm

Finally, the shaft connecting these two machines has the following parameters shown in table C.3.

Table C.3: Parameters of the shaft connecting the two machines.

Parameter name	Symbol	Value
Moment of inertia	J	0.192 kgm^2
Friction coefficient	f	0.057 Nms

D Transformations

This appendix details the calculus related to the EMR transformation element and has two parts. First, the machine connection type is considered as a factor determining how given inverter voltages and currents are converted into machine phase voltages and currents, and vice versa. Second, the Park transformation and the inverse transformation are derived. They describe conversions between machine phase quantities and space vectors in a rotating coordinate system.

Machine connection type

The definitions of star and delta connections with related voltage and current directions as used in this work are shown in figure D.1 with subindex numbers indicating inverter quantities and letters machine phase quantities.
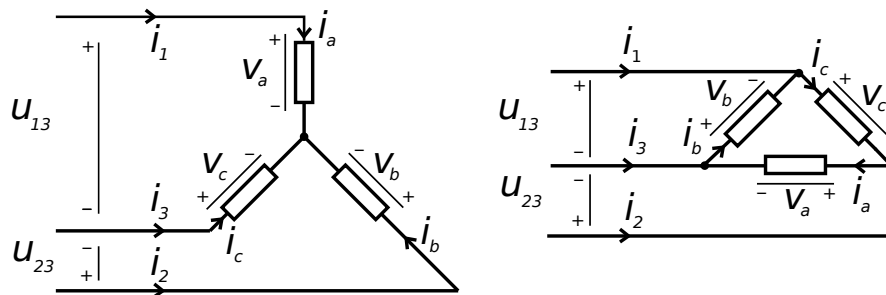

Figure D.1: Used definition of star and delta connections of machine phases.

Considering the machine phase voltages and currents to form sets of three-phase systems (sum of phase quantities equal to zero), the connection definitions of figure D.1 yield the transformation matrices given below.

Inverter line-to-line voltages to machine phase voltages:

$$
\begin{bmatrix} v_a \\ v_b \\ v_c \end{bmatrix} = [T_{uv}] \begin{bmatrix} u_{13} \\ u_{23} \end{bmatrix}, \quad \text{with} \begin{cases} \text{Star connection:} [T_{uv}] = \frac{1}{3} \begin{bmatrix} 2 & -1 \\ -1 & 2 \\ -1 & -1 \end{bmatrix} \\ \text{Delta connection:} [T_{uv}] = \begin{bmatrix} 0 & 1 \\ -1 & 0 \\ 1 & -1 \end{bmatrix} \end{cases} \quad \text{[(D)-1]}
$$

Machine phase voltages to inverter line-to-line voltages:

$$
\begin{bmatrix} u_{13} \\ u_{23} \end{bmatrix} = [T_{vu}] \begin{bmatrix} v_a \\ v_b \\ v_c \end{bmatrix}, \quad \text{with} \begin{cases} \text{Star connection: } [T_{vu}] = \begin{bmatrix} 1 & 0 & -1 \\ 0 & 1 & -1 \end{bmatrix} \\ \text{Delta connection: } [T_{vu}] = \begin{bmatrix} 0 & -1 & 0 \\ 1 & 0 & 0 \end{bmatrix} \end{cases} \qquad \text{[(D)-2]}
$$

Inverter line currents to machine phase currents:

$$
\begin{bmatrix} i_a \\ i_b \\ i_c \end{bmatrix} = [T_i] \begin{bmatrix} i_1 \\ i_2 \end{bmatrix}, \quad \text{with} \begin{cases} \text{Star connection: } [T_i] = \begin{bmatrix} 1 & 0 \\ 0 & 1 \\ -1 & -1 \end{bmatrix} \\ \text{Delta connection: } [T_i] = \frac{1}{3} \begin{bmatrix} 1 & 2 \\ -2 & -1 \\ 1 & -1 \end{bmatrix} \end{cases} \qquad \text{[(D)-3]}
$$

Machine phase currents to inverter line currents:

$$
\begin{bmatrix} i_1 \\ i_2 \end{bmatrix} = [T_{ii}] \begin{bmatrix} i_a \\ i_b \\ i_c \end{bmatrix}, \quad \text{with} \begin{cases} \text{Star connection: } [T_{ii}] = \begin{bmatrix} 1 & 0 & 0 \\ 0 & 1 & 0 \end{bmatrix} \\ \text{Delta connection: } [T_{ii}] = \begin{bmatrix} 0 & -1 & 1 \\ 1 & 0 & -1 \end{bmatrix} \end{cases} \qquad \text{[(D)-4]}
$$

Park transformation

The approach taken in this work takes use of the mathematical tool of a space vector. This involves describing a symmetric three-phase system with an equivalent two-phase system, as the three-phase symmetry leads to the presence of only two independent quantities. The complex plane is used in order to represent this two-phase system with a single complex quantity. These operations are accomplished with the space vector definition [42]

$$
\underline{s}_{\alpha_s \beta_s}(t) = \frac{2}{3} K \left[s_a(t) + s_b(t) e^{\frac{j2\pi}{3}} + s_c(t) e^{\frac{j4\pi}{3}} \right] \qquad \text{[(D)-5]}
$$

where $s_a(t)$, $s_b(t)$ and $s_c(t)$ are the set of symmetrical three phase quantities and $\underline{s}_{\alpha_s \beta_s}(t)$ the corresponding space vector. The scaling constant K is chosen throughout this work as $K = \sqrt{\frac{3}{2}}$. This results in the instantaneous power of a three-phase system being given as [39]

$$p(t) = \Re\{\underline{u}\underline{i}^*\} \qquad \text{[(D)-6]}$$

Another choice of K would necessitate the addition of scaling constants to obtain the same power value. The space vector definition of [(D)-5] produces a space vector in the stationary stator coordinates as defined in figure 3.2. Transformations of type

$$\underline{s}_x = \underline{s}_{\alpha_s \beta_s} \underline{e}^{-j\theta_x} \quad \text{From stator coordinates to coordinate system } x \qquad \text{[(D)-7a]}$$

$$\underline{s}_{\alpha_s \beta_s} = \underline{s}_x \underline{e}^{j\theta_x} \quad \text{From coordinate system } x \text{ to stator coordinates} \qquad \text{[(D)-7b]}$$

can be used in order to move from one coordinate system to another. Here, the general coordinate system x is characterized by the transformation angle θ_x (compare with angles defined in figure 3.2). By combining the space vector definition of equation [(D)-5], the coordinate transformation of [(D)-7a] and Euler's formula

$$\underline{e}^{-j\gamma} = cos(\gamma) - jsin(\gamma) \qquad \text{[(D)-8]}$$

the Park transformation of equation [(D)-9] is obtained. The inverse Park transformation of equation [(D)-10] can be derived in a similar fashion. First, a transformation of type [(D)-7b] is used to move from rotating coordinate system x to stator coordinates after which the space vector is divided into phase quantities.

$$\underline{s}_x = \begin{bmatrix} s_{\alpha_x} \\ s_{\beta_x} \end{bmatrix} = \sqrt{\frac{2}{3}} \underbrace{\begin{bmatrix} \cos(\theta_x) & \cos(\theta_x - \frac{2\pi}{3}) & \cos(\theta_x + \frac{2\pi}{3}) \\ -\sin(\theta_x) & -\sin(\theta_x - \frac{2\pi}{3}) & -\sin(\theta_x + \frac{2\pi}{3}) \end{bmatrix}}_{\left[T(\theta_{d/s})_{PARK}\right]} \begin{bmatrix} s_a \\ s_b \\ s_c \end{bmatrix} \qquad \text{[(D)-9]}$$

$$\begin{bmatrix} s_a \\ s_b \\ s_c \end{bmatrix} = \sqrt{\frac{2}{3}} \underbrace{\begin{bmatrix} \cos(\theta_x) & -\sin(\theta_x) \\ \cos(\theta_x - \frac{2\pi}{3}) & -\sin(\theta_x - \frac{2\pi}{3}) \\ \cos(\theta_x + \frac{2\pi}{3}) & -\sin(\theta_x + \frac{2\pi}{3}) \end{bmatrix}}_{\left[T(\theta_{d/s})_{PARK}\right]^{-1}} \begin{bmatrix} s_{\alpha_x} \\ s_{\beta_x} \end{bmatrix} \qquad \text{[(D)-10]}$$

E   Closed-loop controller design

The emulation platform of figure 3.8 shows that five indirect inversions (light blue elements with diagonal bars), i.e. closed-loop controllers are required. Furthermore, the stator current controllers of both machines are vector-valued and thus necessitate two scalar-valued controllers for the implementation of each space vector controller. The use of EMR does not set any special requirements for the implementation of the closed-loop controllers. In this work, PI controllers are used for all closed-loop controller implementations. The block diagram of a PI controller controlling a general first-order system is shown below in figure E.1. In the most simple case, the controller output u_{ref} can be directly actuated to the process input value u, i.e. $u = u_{ref}$. However, this is not the case for any of the emulation platform's closed-loop controllers[27]. Nevertheless, in the design of the controller it is assumed that $u = u_{ref}$. This assumption needs to be carefully examined especially when other closed-loop controllers are involved in actuating u_{ref} into u. In this case, *cascade control* is formed and it is important that the inner closed-loop controller has a significantly shorter response time than the outer controller[28].
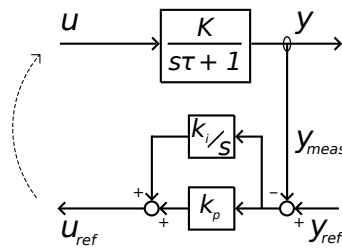

Figure E.1: Control of a first-order system by a PI controller.

The design of a PI controller involves most importantly the choice of controller parameters k_p and k_i. This can be done in a systematic fashion by forming transfer function y/y_{ref} of the controlled system shown in figure E.1. The resulting second-order transfer function's denominator is then compared to the denominator of a general second-order system, as shown in equation [(E)-1]. Consequently, conditions can be formed for the controller parameters based on the desired response dynamics determined by the damping ratio ξ and natural frequency ω_n. However, this way of design

---

[27]This can be seen from the EMR diagram of figure 3.8 where none of the indirect inversion blocks yield variables that are directly actuated.

[28]An example of this can be taken from the emulation platform's PMSM speed drive. The outer speed PI controller outputs torque reference $T_{sm,ref}$ whose actuation involves the PI controllers of the stator currents. Thus, the stator current controllers need to be significantly faster than the shaft speed controller. This separation of time scales enables the speed controller to consider $T_{sm,ref} = T_{sm}$ without significant error.

neglects the effect of the PI controller transfer function's zero. Therefore, the actual closed-loop response will not correspond exactly to the dynamics chosen with ξ and ω_n.

$$\frac{y}{y_{ref}} = \frac{\frac{sk_pK+k_iK}{\tau}}{s^2 + s\frac{1+k_pK}{\tau} + \frac{k_iK}{\tau}} = \frac{numerator}{s^2 + 2\xi\omega_ns + \omega_n^2}, \implies \begin{cases} k_p = \frac{2\xi\omega_n\tau-1}{K} \\ k_i = \frac{\omega_n^2\tau}{K} \end{cases} \qquad \text{[(E)-1]}$$

Another possibility exists for designing the response transfer function. The closed-loop transfer function's zero can also be used to compensate one of the poles, thus resulting in a first-order closed-loop transfer function. This yields the conditions shown in equation [(E)-2] with τ_{cl} defined as the time constant of the closed-loop response.

$$\frac{y}{y_{ref}} = \frac{1}{\frac{1}{(k_p+\frac{k_i}{s})(\frac{K}{s\tau+1})} + 1} = \frac{1}{s\tau_{cl} + 1}, \implies \begin{cases} k_p = \tau k_i \\ k_i = \frac{1}{K\tau_{cl}} \end{cases} \qquad \text{[(E)-2]}$$

In addition, in digital implementations a numeric integration method must be chosen to implement the controller integrator part. In this work, all numeric integrations used in the platform are performed with the simple *forward Euler* method

$$H_n = H_{n-1} + h_{n-1}T_{stepsize} \qquad \text{[(E)-3]}$$

where h is the discrete function to be integrated, H is the function's integral, $T_{stepsize}$ the length of the time step and n is the sample index. Despite the simplicity of the method, the integral error remains minor if the time step size is small.

One more major consideration exists in the design of the closed-loop controllers - the addition of output saturation and integrator *anti-windup* into the controllers. Saturating the controller output can be necessary in order to prevent generating control references that are unsafe or that simply cannot be actuated in reality. For example, the closed-loop current control of the induction machine stator currents outputs a stator voltage space vector reference. However, there is an upper limit to the magnitude of the voltage space vector that can be realized. This limit depends on the DC voltage supplying the inverter and the PWM strategy that is used to convert the DC voltage into a set of AC voltages. Saturating the control output of the current controller prevents passing on a voltage instruction that cannot be realized[29]. However, this presents a new problem in the control. As described above, the PI controllers

---

[29]If this saturation is not performed with the control signals, it will occur physically once the inverter modulation function reaches its limit values.

employ an integrator block whose gain parameter k_i is selected based on the desired response. However, if the controller output cannot be realized, the designed response dynamics will not be achieved. In practice, saturation leads to a slower response. This has unfortunate effects on the integrator of the controller because it keeps integrating the control error according to its design without knowledge that the system is at its limits and can no longer follow the designed dynamics. Typically, this results in large overshoots and long settling times in the closed-loop response. The purpose of the controller anti-windup is to protect against this by modifying the integration process in one way or another when saturation occurs. The anti-wind up scheme used in this work is the so called *back calculation anti-windup*[30][39] , shown in figure E.2. The scheme is based on modifying the integrator input when saturation occurs. In case of saturation, the integrator is made to operate on a modified control error e_i that would have generated a control output on the saturation limit (instead of over it). This is accomplished by a feedback from the difference between the unsaturated and saturated control outputs through the back-calculation coefficient gain $1/k_p$.
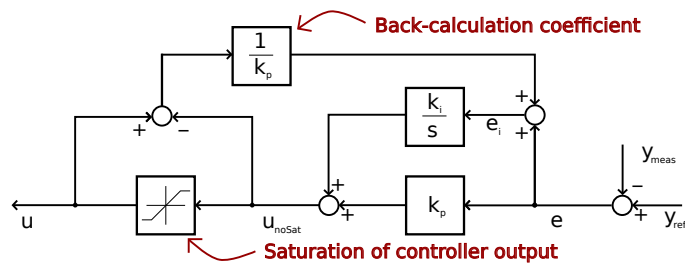

Figure E.2: Back-calculation anti-windup for a PI controller.

Table E.1 shows the closed-loop controller parameters used in the emulation platform. The preferred tuning method for the controllers was equation [(E)-2] because the first-order closed-loop response is typically less prone to overshooting than if equation [(E)-1] is used to design a fast second order response[31]. Manual tuning was used for the design of the PMSM shaft speed controller, i.e. the coefficients were determined experimentally. Small variations of these parameters were found to have significant effects on the emulation platform's performance and thus improvements in controller performance were seeked by experimentally varying the controller parameters.

Anti-windups as shown in figure E.2 were implemented for the current control of

---

[30]A comparison of this anti-windup scheme with other methods is presented in [43].

[31]The response type obviously depends crucially on the chosen response characteristics (τ_{cl} for first order response, ξ and ω_n for second order response). However, the transfer function zero that is neglected when using [(E)-1] typically results in increased overshooting that is not anticipated with the design equation.

Table E.1: Closed-loop controller parameters used in the emulation platform.

Controller	Tuning	k_p	k_i	Saturation limit
IM eq. winding d current	[(E)-2]	8.82	105	$\underline{v}_{s,dq,lim} = 0.65 u_{bat,meas}$
IM eq. winding q current	[(E)-2]	8.82	105	$\underline{v}_{s,dq,lim} = 0.65 u_{bat,meas}$
Rotor flux	[(E)-1]	82.6	2249	None
Equivalent chassis	[(E)-2]	207.3	12.76	None
PMSM shaft speed	Manual	9.60	0.285	None
PMSM stator d current	[(E)-2]	4.86	246	$\underline{v}_{sm,s,dq,lim} = 0.65 u_{sm,bus,meas}$
PMSM stator q current	[(E)-2]	6.06	246	$\underline{v}_{sm,s,dq,lim} = 0.65 u_{sm,bus,meas}$

both machines. These current controllers have an added layer of complexity relating to the saturation of the control output. For example, the IM current controller outputs voltage space vector reference $\underline{v}_{s,dq,ref}$ that consists of the space vector's d and q components. These two component references are given by separate scalar-valued PI controllers but the two-dimensional space vector they form must be saturated in a unified way[32]. In the current controllers of the emulation platform, priority is given to the flux control of the machines. This signifies that if the voltage space vector magnitude is too great, the torque-producing q component is reduced until the entire space vector length becomes realizable. In other words, the d component is not saturated[33]. The remaining issue is then to determine the correct saturation limit for the voltage space vector, i.e. to determine the maximum realizable space vector magnitude. It is recalled that the voltage space vector magnitude is proportional to the amplitude of the machine stator three-phase voltages. Consequently, it depends on the DC voltage supplying the inverter and the PWM strategy that is used to convert the DC voltage into a set of AC voltages. It was experimentally determined for the emulation platform that the modulation function of the inverter reaches its limit values when the voltage space vector magnitude is approximately 70% of the inverter DC voltage. In order to saturate the space vector reference before this occurs, a limit of 65% of the DC bus voltage was used to saturate the voltage space vector. The equivalent chassis and PMSM shaft speed controllers do not include saturation blocks because the speeds are determined by the drive cycle and thus the references need to be followed without significant delay. The IM rotor flux controller does not require anti-windup because the controller's output $i_{sd,ref}$ is given priority in the IM current control and thus the reference can be reached without saturation occuring.

---

[32]If the two components are saturated separately, there is a high likelyhood of a resulting voltage space vector whose magnitude is less than what is possible to realize with the inverter. In contrast, saturating the voltage space vector as a unified quantity allows forming a space vector reference whose magnitude is the maximum realizable value.

[33]Another conceivable method would be to saturate both the d and q components of the voltage space vector. However, reducing the d component in this way would lead to undesired flux weakening every time the current controller saturates.

F   Field weakening operation

The achievable speed range of an induction machine can be significantly extended with field weakening operation of the machine. This signifies lowering the flux magnitude in order to reach higher rotation speeds. This is seen in the efficiency map of figure 2.4 at vehicle speeds higher than approximately $8.1m/s$. It is the goal of this appendix to describe the flux weakening of the emulation platform's induction machine.

The physical background of flux weakening can be understood from the model equations of the machine. From [(3)-14] it is observed that the back emf's of the machine increase with the stator angular frequency $\omega_{d/s}$ and the rotor flux magnitude Φ_{rd}. Equation [(3)-13] shows that the increasing of the back emf's creates a larger resistive voltage disturbance for the stator current control of i_{sd} and i_{sq}. Thus, the more the rotation speed and thereby the stator angular frequency increase, the higher the stator voltage requirement becomes to reach given stator current component values. It is recalled from equations [(3)-16] and [(3)-17] that the control of these current components is directly proportional to the flux and torque control of the machine. However, in practice the stator voltages cannot be increased beyond a certain value. On the other hand, equation [(3)-14] informs that by lowering the rotor flux magnitude, the back emf's decrease. This is the basis of flux weakening operation. At high speeds, the increase of the back emf's is avoided by lowering the rotor flux magnitude. However, flux weakening comes with a major disadvantage. As can be seen from equation [(3)-16], the torque of the machine is proportional to the rotor flux magnitude. Therefore, weakening the flux decreases also the torque-producing capability of the machine. This is why flux weakening should only be used when necessary. It also explains the Tazzari Zero's reduced tractive force capability at high speeds, visible in figure 2.4 at elevated speeds of the vehicle.

Understanding the fundamental mechanisms by which the rotor flux magnitude affects the speed and torque capability of the machine, focus is now given to controlling it. Two main issues need to be resolved to establish the rotor flux control strategy of the machine. First, the nominal rotor flux value needs to be calculated. This is used as the flux reference value at low speeds when flux weakening is not necessary. This value is usually not given by the machine manufacturer. Second, an appropriate method for decreasing the flux at high speeds needs to be determined.

First, the nominal rotor flux value is computed. As described by equation [(3)-17], the rotor flux magnitude Φ_{rd} is controlled by the stator current component i_{sd}. Thus, if the nominal value of this current component can be calculated, the corresponding

nominal rotor flux value is obtained from this equation in steady state, i.e.

$$\Phi_{rd,nom} = M_{sr} i_{sd,nom} \qquad \text{[(F)-1]}$$

The nominal current d component value $i_{sd,nom}$ can be obtained as follows. First, equations [(3)-10] and [(3)-11] are written in the nominal steady state operating point. It is assumed that at the nominal point the voltage drop over the stator resistance is small compared to other terms, yielding

$$\begin{cases} v_{sd,nom} = \omega_{d/s,nom}(\dfrac{M_{sr}^2}{L_r} - L_s)i_{sq,nom} \\[2mm] v_{sd,nom} = \omega_{d/s,nom} L_s i_{sd,nom} \end{cases} \qquad \text{[(F)-2]}$$

Combining this with conditions

$$\begin{cases} |\underline{v}_{s,nom}|^2 = v_{sd,nom}^2 + v_{sq,nom}^2 \\[2mm] |\underline{i}_{s,nom}|^2 = i_{sd,nom}^2 + i_{sq,nom}^2 \end{cases} \qquad \text{[(F)-3]}$$

yields the nominal stator d current component as

$$i_{sd,nom} = \sqrt{ |\underline{i}_{s,nom}|^2 - \frac{(\frac{|v_{s,nom}|}{\omega_{d/s,nom}})^2 - (L_s|\underline{i}_{s,nom}|)^2}{\frac{M_{sr}^4}{L_r^2} - \frac{2L_s M_{sr}^2}{L_r}} } \qquad \text{[(F)-4]}$$

Equations [(F)-1] and [(F)-4] can then be used to compute the nominal rotor flux value. This requires knowledge of the nominal values of the voltage and current space vectors $|\underline{v}_{s,nom}|$ and $|\underline{i}_{s,nom}|$ as well as the nominal stator angular frequency $\omega_{d/s,nom}$. These can be easily obtained from the IM nameplate data (see appendix C). With scaling constant K in the space vector definition of equation [(D)-5] chosen as $K = \sqrt{\frac{3}{2}}$ (see appendix D), the nominal voltage and current RMS values given in the nameplate data are equal to the respective nominal space vector magnitudes. Consequently, for the IM of the emulation platform, the nominal rotor flux magnitude is obtained as $\Phi_{rd,nom} = 1.15Wb$.

Next, it is considered how the rotor flux magnitude should be modified in order to reach higher rotation speeds. In this work, the following approach is taken. The rotor flux is decreased as the inverse of the speed increase above the base rotation speed[34], i.e.

---

[34]The base rotation speed $\Omega_{sh,base}$ is the rotation speed at which flux weakening is begun.

$$\Phi_{rd,ref} = \begin{cases} \Phi_{rd,nom}, & |\Omega_{sh}| \leq \Omega_{sh,base} \\ \Phi_{rd,nom}\frac{\Omega_{sh,base}}{\Omega_{sh}}, & |\Omega_{sh}| > \Omega_{base} \end{cases} \qquad \text{[(F)-5]}$$

With the parameters of the emulation platform's IM, the resulting flux weakening strategy used in this work is shown in figure F.1. The base speed has been chosen as $\Omega_{sh,base} = 89rad/s$ for a DC bus level of about 230V for the IM. This was found to result in satisfactory field weakening so that desired speeds could be reached.
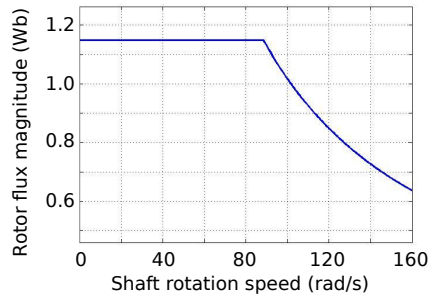

Figure F.1: Flux weakening strategy used in this work for the IM.

Flux weakening usage in emulation is demonstrated below in figure F.2. The figure shows how at speeds above the base speed, the flux is controlled to a lower value.
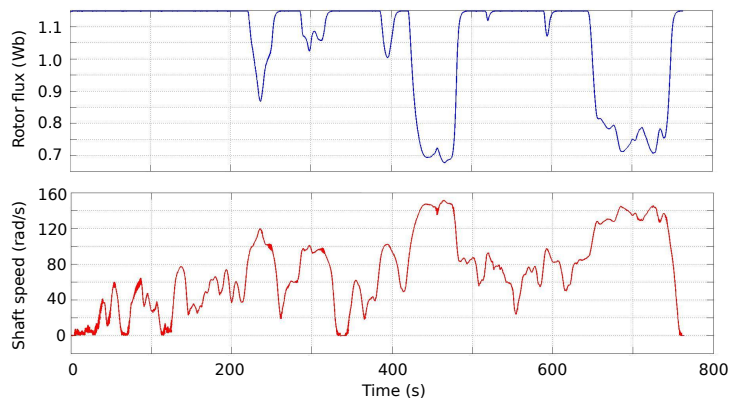

Figure F.2: Usage of flux weakening during emulation.

The advantage of this method is its simplicity and rather good performance. However, it does not result in maximal torque-producing capability in the field weakening region [44]. A more advanced method that provides this capability and that is insensitive to errors in machine parameters has been proposed in [45]. However, these properties come at the cost of two additional PI controllers. Therefore, in this work the simple flux weakening strategy shown in figure F.1 is used.

G   Symmetrical suboscillation PWM

The mechanism for controlling the emulation platform of figure 3.8 is the control of the switching orders of the two inverters of the system. The induction machine drive's VSI and its control element[35] are represented by EMR as shown below in figure G.1 .
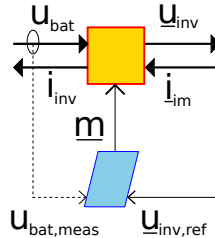

Figure G.1: VSI and related control element.

The first step to obtaining appropriate switching orders is reformulating the VSI's model equation [(3)-1] into

$$\underline{m}_{ave} = \frac{\underline{u}_{inv,ref}}{u_{bat,meas}} \qquad \text{[(G)-1]}$$

However, the result of this operation does not yield directly usable switching orders. This is due to two reasons. First, the control law [(G)-1] results in continuous real number values for $\underline{m}_{ave}$ that are not directly applicable to the VSI switches. This is because the switches can only either be in the conducting state or in the non-conducting state. Indeed, $\underline{m}_{ave}$ represents the desired average switching orders while the actual instantaneous values need to be obtained by means of Pulse Width Modulation (PWM). The PWM can be implemented by the traditional method of comparing the desired average switching order values to triangular carrier waves of high frequency [39]. This well-known triangular wave comparison is not further detailed here. Second, the actual inverter switching orders are the three[36] switching orders $\{s_{11}, s_{21}, s_{31}\}$, not the two elements of the modulation function $\underline{m}$ as defined by equation [(3)-1]. Thus, the first goal of this appendix is showing how to obtain these three switching orders from a given modulation function. The second goal is to present the *symmetrical suboscillation method*. This method allows taking maximal advantage of the available DC voltage by modifying the switching orders in a specific way.

First, it is considered how the desired average modulation function $\underline{m}_{ave}$ can be trans-

---

[35]Here notation for the IM drive's inverter is used but the same concept is used for the PMSM drive's inverter.

[36]As explained in section 3, the three switching orders of the remaining three lower semiconductor switches $\{s_{12}, s_{22}, s_{32}\}$ are obtained as the complements of the switching orders of the upper switches.

formed into three switching orders $\{s_{11}, s_{21}, s_{31}\}$. This is done for the inverter shown below in figure G.2. The inverter of the figure is identical to that of figure 3.1 except for the addition of a reference earth whose potential level is chosen to be the middle point of the voltage between the battery terminals. Fictitous inverter phase voltages can then be defined as voltages from each inverter line to this reference earth potential. It is emphasized that neither these inverter phase voltages nor the reference earth are physically relevant but that they are only used as a tool for obtaining the switching order values.
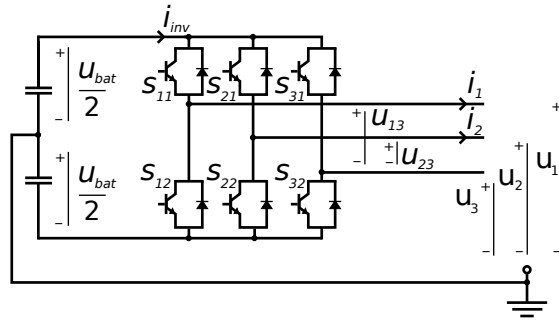

Figure G.2: VSI with fictitous phase voltages shown.

As before, switching order value 1 signifies conducting state of the switch while -1 signifies non-conducting state. Combining this definition with the condition that the fictitous phase voltages should form a set of three-phase voltages ($u_1 + u_2 + u_3 = 0$), the switching order values can be obtained as

$$\begin{bmatrix} s_{11} \\ s_{21} \\ s_{31} \end{bmatrix} = \frac{2}{3} \begin{bmatrix} 2 & -1 \\ -1 & 2 \\ -1 & -1 \end{bmatrix} \underline{m}_{ave} \qquad \text{[(G)-2]}$$

Using equation [(G)-2] to compute the switching order values results in switching orders that vary sinusoidally in steady state[37]. This is the basic approach to determining the switching orders. However, this approach does not take maximal advantage of the DC bus because overmodulation [39] is never used. A more advanced method is the symmetrical suboscillation method [46]. The key idea of the method is to add a zero-sequence component into the switching orders, i.e. to add the same term at all instants of time into each of the three individual switching orders. This then results in zero-sequence components appearing also in the machine phase voltages. Interestingly, this can be done without effect on the currents of the machine.

---

[37]Once again, it is noted that these continuous-valued signals are then implemented approximately by means of the triangular wave comparison.

The reason for this is that in the absence of a neutral connector in the machine, the zero-sequence voltage component cannot induce currents as there is no return path for the zero-sequence current component. This idea has typically been utilized by adding 3rd harmonic content or other zero-sequence components to the switching signals [39, 47]. In contrast to this concept of adding specific harmonic content to the switching orders, the symmetrical suboscillation method is based on choosing the zero-sequence component at each instant according to

$$\Delta = \frac{max\{s_{11}, s_{21}, s_{31}\} + min\{s_{11}, s_{21}, s_{31}\}}{2}$$
[(G)-3]

Adding Δ to the original switching orders obtained from [(G)-2] results in the zero level being exactly in the middle point between the largest and the smallest switching order values. Balancing the switching order values symmetrically around the zero level in this fashion has the effect of the switching orders reaching the limit values of 1 and -1 only when it can no longer be avoided by overmodulation. In this way, for a given battery voltage level, the inverter's capacity to create AC voltages of maximum possible amplitude is obtained.

The results of this appendix are summarized by equation [(G)-4]. It describes how the switching orders are obtained from the desired average modulation function $\underline{m}_{ave}$ by using the symmetrical suboscillation method. In the equation, Δ is chosen according to [(G)-3].

$$\begin{bmatrix} s'_{11} \\ s'_{21} \\ s'_{31} \end{bmatrix} = \frac{2}{3} \begin{bmatrix} 2 & -1 \\ -1 & 2 \\ -1 & -1 \end{bmatrix} \underline{m}_{ave} + \begin{bmatrix} \Delta \\ \Delta \\ \Delta \end{bmatrix}$$
[(G)-4]

The entire contents of the light blue control block shown in figure G.1 are summarized below in figure G.3[38].
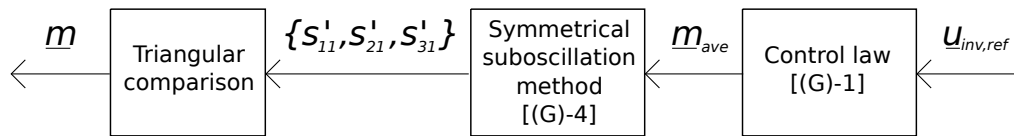

Figure G.3: Control of a VSI.

[38]It is noted that the triangular comparison results in the three realizable switching order values that indicate the respective switch to be either in the conducting or the non-conducting state. From these, the other three switching orders $\{s_{12}, s_{22}, s_{32}\}$ can be obtained as the respective complement values. For a real VSI, the six obtained realizable switching orders are the required control signals and are given to the driver circuits of the switches. In other words, they are not collected back into the modulation function $\underline{m}$. This is done in the EMR diagrams for compactness.

References

[1] C. C. Chan. The state of the art of electric, hybrid, and fuel cell vehicles. *Proceedings of the IEEE*, 95(4):704–718, 2007.

[2] M. Ehsani, Y. Gao, and A. Emadi. *Modern Electric, Hybrid Electric, and Fuel Cell Vehicles*. CRC Press, 2nd edition, 2009.

[3] C. Dépature, W. Lhomme, A. Bouscayrol, P. Sicard, and L. Boulon. Efficiency map of the traction system of an electric vehicle from an on-road test drive. *IEEE Vehicle Power and Propulsion Conference, Coimbra*, pages 1–6, 2014.

[4] D. Maclay. Simulation gets into the loop. *IEE Review*, 43(3):109–12, 1997.

[5] A. Bouscayrol. *Industrial Electronics Handbook*. Editions Taylor & Francis, Chicago, 2 edition, 2011.

[6] A. Bouscayrol, J. P. Hautier, and B. Lemaire-Semail. *Graphic Formalisms for the Control of Multi-Physical Energetic Systems*. ISTE Wiley Editions, 1st edition, 2012.

[7] IPCC. Climate change 2014 synthesis report. *IPCC*, 2014.

[8] F. Zhong, O. Martinez, R. Gormus, and P. Kulkarni. The reign of EV's? An economic analysis from consumer's perspective. *IEEE Electrification Magazine*, 2(2):61–71, 2014.

[9] M. Messagie, C. Macharis, and J. Van Mierlo. Key outcomes from life cycle assessment of vehicles, a state of the art literature review. *Electric Vehicle Symposium and Exhibition (EVS27), Barcelona*, pages 1–9, 2013.

[10] M. Messagie, F.-S. Boureima, T. Coosemans, C. Macharis, and J. Van Mierlo. A range-based vehicle life cycle assessment incorporating variability in the environmental assessment of different vehicle technologies and fuels. *MDPI energies*, 7(3):1467–1482, 2013.

[11] Ecolane Transport Consultancy. Life cycle assessment of vehicle fuels and technologies. *Final Report London Borough of Camden*, 2006.

[12] Eurelectric. The role of electricity, a new path to secure competitive energy in a carbon-constrained world. *Eurelectric*, 2007.

[13] B. Frieske, M. Kloetzke, and F. Mauser. Trends in vehicle concept and key technology development for hybrid and battery electric vehicles. *Electric Vehicle Symposium and Exhibition (EVS27), Barcelona*, pages 1–12, 2013.

[14] International Energy Agency (IEA). Technology Roadmap: Electric and Plug-in Hybrid Electric Vehicles (EV/PHEV). *IEA*, 2011.

[15] A. Affani, A. Bellini, G. Franceschini, P. Guglielmi, and C. Tassoni. Battery choice and management for new-generation electric vehicles. *IEEE Transactions on Industrial Electronics*, 52(5):1343–1349, 2005.

[16] M. Yilmaz and P. T. Krein. Review of Battery Charger Topologies, Charging Power Levels, and Infrastructure for Plug-In Electric and Hybrid Vehicles. *IEEE Transactions on Power Electronics*, 28(5):2151–2169, 2012.

[17] A. Hoke, A. Brissette, K. Smith, A. Pratt, and D. Maksimovic. Accounting for Lithium-Ion Battery Degradation in Electric Vehicle Charging Optimization. *IEEE Journal of Emerging and Selected Topics in Power Electronics*, 2(3):691–700, 2014.

[18] V. V. Viswanathan and M. Kintner-Meyer. Second Use of Transportation Batteries: Maximizing the Value of Batteries for Transportation and Grid Services. *IEEE Transactions on Vehicular Technology*, 60(7):2963–2970, 2014.

[19] D. W. Gao, C. Mi, and A. Emadi. Modeling and Simulation of Electric and Hybrid Vehicles. *Proceedings of the IEEE*, 95(4):729–745, 2007.

[20] A.-L. Allègre, A. Bouscayrol, J.-N. Verhille, P. Delarue, E. Chattot, and S. El-Fassi. Reduced-scale-power hardware-in-the-loop simulation of an innovative subway. *IEEE Transactions on Industrial Electronics*, 57(4):1175–1185, 2010.

[21] J. Bauman and M. Kazerani. A Comparitive Study of Fuel-Cell-Battery, Fuel-Cell-Ultracapacitor, and Fuel-Cell-Battery-Ultracapacitor Vehicles. *IEEE Transactions on Vehicular Technology*, 57(2):760–769, 2008.

[22] A. Khaligh and L. Zhihao. Battery, ultracapacitor, fuel cell, and hybrid energy storage systems for electric, hybrid electric, fuel cell, and plug-in hybrid electric vehicles: State of the art. *IEEE Transactions on Vehicular Technology*, 59(6):2806–2814, 2010.

[23] Tazzari zero website. `http://www.tazzari-zero.com`. Accessed: 2015-01-31.

[24] S. S. Williamson, S. M. Lukic, and A. Emadi. Comprehensive drive train efficiency analysis of hybrid electric and fuel cell vehicles based on motor-controller efficiency modeling. *IEEE Transactions on Power Electronics*, 21(3):730–740, 2006.

[25] W. Deprez, D. Lemmens, D. Vanhooydonck, W. Symens, K. Stockman, S. Dereyne, and J. Driesen. Iso efficiency contours as a concept to characterize variable speed drive efficiency. *XIX International Conference on Electrical Machines, Rome*, pages 1–6, 2010.

[26] IEEE standard test procedure for polyphase induction motors and generators. *IEEE Std. 112-2004*, 2004.

[27] K. Stockman, S. Dereyne, D. Vanhooydonck, W. Symens, J. Lemmens, and W. Deprez. Iso efficiency contour measurement results for variable speed drives. *XIX International Conference on Electrical Machines, Rome*, pages 1–6, 2010.

[28] C. A. Rabbath, M. Abdoune, J. Belanger, and K. Butts. Simulating Hybrid Dynamic Systems. *IEEE Robotics & Automation Magazine*, 9(2):39–47, 2002.

[29] H. Paynter. *Analysis and design of engineering systems*. MIT Press, 1961.

[30] J. P. Hautier and P. J. Barre. The causal ordering graph - a tool for modelling and control law synthesis. *Studies in Informatics and Control Journal*, 13(4):265–283, 2004.

[31] A. Bouscayrol, B. Davat, B. de Forner, B. François, J. P. Hautier, F. Meibody-Tabar, E. Monmasson, M. Pietrzak-David, H. Razik, E. Semail, and F. Benkhoris. Control structures for multi-machine multi-converter systems with upstream coupling. *Mathematics and computers in simulation*, 63(3-5):261–270, 2003.

[32] EMR website. `http://www.emrwebsite.org`. Accessed: 2015-01-31.

[33] W. Lhomme, R. Trigui, P. Delarue, B. Jeanneret, A. Bouscayrol, and F. Badin. Switched Causal Modeling of Transmission With Clutch in Hybrid Electric Vehicles. *IEEE Transactions on Vehicular Technology*, 57(4):2081–2088, 2012.

[34] L. Boulon, A. Bouscayrol, D. Hissel, O. Pape, and M.-C. Pèra. Inversion-based control of a highly redundant military hev. *IEEE Transactions on Vehicular Technology*, 62(2):500–510, 2013.

[35] L. Boulon, D. Hissel, A. Bouscayrol, and M.-C. Pèra. From modeling to control of a pem fuel cell using energetic macroscopic representation. *IEEE Transactions on Industrial Electronics*, 57(6):1882–1891, 2010.

[36] A. Bouscayrol, X. Guillaud, P. Delarue, and B. Lemaire-Semail. Energetic macroscopic representation and inversion-based control illustrated on a wind-energy-

conversion system using hardware-in-the-loop simulation. *IEEE Transactions on Industrial Electronics*, 56(12):4826–4835, 2009.

[37] C. Mayet, J. Pouget, A. Bouscayrol, and W. Lhomme. Influence of an energy storage system on the energy consumption of a diesel-electric locomotive. *IEEE Transactions on Vehicular Technology*, 63(3):1032–1040, 2014.

[38] T. Letrouvé, W. Lhomme, A. Bouscayrol, and N. Dollinger. Control validation of Peugeot3∞8 Hybrid4 Vehicle Using a Reduced-scale Power HIL Simulation. *Journal of Electrical Engineering and Technology*, 8(5):1227–1233, 2013.

[39] L. Harnefors. *Control of Variable-Speed Drives*. Västerås, Sweden: Applied Signal Processing and Control, Department of Electronics, Mälardalen University, 2003.

[40] A. Castaings, W. Lhomme, R. Trigui, and A. Bouscayrol. Different control schemes of a battery/supercapacitor system in electric vehicle. *IEEE Vehicle Power and Propulsion Conference, Coimbra*, pages 1–6, 2014.

[41] C. Dépature, A. Bouscayrol, and L. Boulon. Range-extender electric vehicle using a fuel cell. *IEEE Vehicle Power and Propulsion Conference, Beijing*, pages 1–6, 2013.

[42] U. Drofenik and J. W. Kolar. Modern and intuitive way of teaching space vector calculus and pwm in an undergraduate course. *Proceedings of the Power Conversion Conference, Osaka*, pages 305–310, 2002.

[43] C. Bohn and D. P. Atherton. An analysis package comparing pid anti-windup strategies. *IEEE Control Systems*, 15(2):34–40, 1995.

[44] S.-H. Kim and S.-K. Sul. Maximum torque control of an induction machine in the field weakening region. *IEEE Transactions on Industry Applications*, 31(4):787–794, 1995.

[45] S.-H. Kim and S.-K. Sul. Voltage control strategy for maximum torque operation of an induction machine in the field-weakening region. *IEEE Transactions on Industrial Electronics*, 44(4):512–518, 1997.

[46] T. Svensson. *On modulation and control of electronic power converters*. PhD Thesis, Chalmers University of Technology, Gothenburg, Sweden, 1988.

[47] J. Holtz. Pulsewidth modulation - a survey. *23rd Annual IEEE Power Electronics Specialist Conference, Toledo*, pages 11–18, 1992.